

# A *Chandra* Survey of the X-ray Properties of Broad Absorption Line Radio-Loud Quasars

B. P. Miller,<sup>1</sup> W. N. Brandt,<sup>1</sup> R. R. Gibson,<sup>2</sup> G. P. Garmire,<sup>1</sup> and O. Shemmer<sup>3</sup>

## ABSTRACT

This work presents the results of a *Chandra* study of 21 broad absorption line (BAL) radio-loud quasars (RLQs). We conducted a *Chandra* snapshot survey of 12 bright BAL RLQs selected from SDSS/FIRST data and possessing a wide range of radio and C IV absorption properties. Optical spectra were obtained nearly contemporaneously with the Hobby-Eberly Telescope; no strong flux or BAL variability was seen between epochs. In addition to the snapshot targets, we include in our sample 9 additional BAL RLQs possessing archival *Chandra* coverage. We compare the properties of (predominantly high-ionization) BAL RLQs to those of non-BAL RLQs as well as to BAL radio-quiet quasars (RQQs) and non-BAL RQQs for context.

All 12 snapshot and 8/9 archival BAL RLQs are detected, with observed X-ray luminosities less than those of non-BAL RLQs having comparable optical/UV luminosities by typical factors of 4.1–8.5. (BAL RLQs are also X-ray weak by typical factors of 2.0–4.5 relative to non-BAL RLQs having both comparable optical/UV and radio luminosities.) However, BAL RLQs are not as X-ray weak relative to non-BAL RLQs as are BAL RQQs relative to non-BAL RQQs. While some BAL RLQs have harder X-ray spectra than typical non-BAL RLQs, some have hardness ratios consistent with those of non-BAL RLQs, and there does not appear to be a correlation between X-ray weakness and spectral hardness, in contrast to the situation for BAL RQQs. RLQs are expected to have X-ray continuum contributions from both disk-corona and small-scale jet emission. While the entire X-ray continuum in BAL RLQs cannot be obscured to the same degree as in BAL RQQs, we calculate that the jet is likely partially

---

<sup>1</sup>Department of Astronomy and Astrophysics, The Pennsylvania State University, 525 Davey Laboratory, University Park, PA 16802; *bmiller, niel, garmire@astro.psu.edu*

<sup>2</sup>Department of Astronomy, University of Washington, Physics-Astronomy Bldg Room C319, Seattle, WA 98195; *rgibson@astro.washington.edu*

<sup>3</sup>Department of Physics, University of North Texas, 1155 Union Circle, #311427, Denton, TX 76203; *ohad@unt.edu*

covered in many BAL RLQs. We comment briefly on implications for geometries and source ages in BAL RLQs.

*Subject headings:* galaxies: active — quasars: absorption lines — galaxies: jets

## 1. Introduction

Quasar outflows help regulate the accretion structure about the central supermassive black hole and propagate kinetic energy into the surrounding environment. Apparently the most extreme manifestation of outflows observed in radio-quiet quasars (RQQs) is the blue-shifted broad absorption lines (BALs) present in the rest-frame UV spectra of  $\simeq 18\text{--}26\%$  of RQQs (e.g., Hewett & Foltz 2003). In an orientation-based unification model, this fraction represents the covering factor of the BAL wind that is common to RQQs. The high polarization within BAL troughs (e.g., Ogle et al. 1999) supports orientation models, while the general IR similarity of BAL and non-BAL RQQs (e.g., Willott et al. 2003; Gallagher et al. 2007) argues against competing “dust-shroud” evolutionary models. BAL RQQs are usually weaker in X-rays than would be expected from their optical luminosities (e.g., Gallagher et al. 2006; Gibson et al. 2009). The X-ray spectra of BAL RQQs show clear evidence of X-ray absorption, often complex, with intrinsic column densities  $N_{\text{H}} > 10^{22} \text{ cm}^{-2}$  (e.g., Gallagher et al. 2002). Although UV and X-ray absorption are clearly linked (e.g., Brandt, Laor, & Wills 2000), the higher column density of the X-ray absorber (e.g., Arav et al. 2003) suggests the X-ray absorption arises interior to the UV BALs, perhaps in the “shielding gas” postulated by Murray et al. (1995) and generated naturally in the simulations of Proga et al. (2000).

A lack of detected BALs in radio-loud<sup>1</sup> quasars (RLQs) led to early suggestions that quasars could possess either a jet, or a BAL wind, but not both simultaneously (e.g., Stocke et al. 1992). However, an increasing number of individual BAL RLQs began to be discovered (e.g., Becker et al. 1997; Brotherton et al. 1998; Wills et al. 1999; Gregg et al. 2000; Ma 2002; Benn et al. 2005), and systematic optical spectroscopic coverage of quasars detected in the VLA 1.4 GHz FIRST survey (Becker et al. 1995) obtained by the FIRST Bright Quasar Survey (FBQS; White et al. 2000) and the Sloan Digital Sky Survey (SDSS; York et al. 2000)

---

<sup>1</sup>We follow the convention that “radio-loudness” ( $R^*$ ) is defined by the ratio of monochromatic luminosities at rest-frame 5 GHz and 2500 Å (e.g., Stocke et al. 1992), where optical/UV luminosities have been corrected for any strong intrinsic reddening. RQQs have  $R^* < 10$  while RLQs require at least  $R^* > 10$ ; we consider objects with  $10 < R^* < 50$  to be radio-intermediate and those with  $R^* > 50$  to be definitively radio-loud.

has increased the number of known radio-loud BAL quasars to  $\gtrsim 100$  (e.g., Becker et al. 2000, 2001; Menou et al. 2001; Shankar et al. 2008). The fraction of quasars with BALs does decrease with increasing radio luminosity (e.g., Shankar et al. 2008). Several of the discovered BAL RLQs have flat or convex radio spectra and/or compact morphologies (e.g., Becker et al. 2000; Liu et al. 2008; Montenegro-Montes et al. 2008), similar to the radio properties of compact steep spectrum (CSS) or GHz peaked spectrum (GPS) radio sources (e.g., O’Dea 1998). The association of BAL RLQs with GPS/CSS radio sources, commonly presumed to be young (e.g., Stawarz et al. 2008 and references therein), has revived evolutionary scenarios (e.g., Gregg et al. 2006), as has the prevalence of objects with low-ionization BALs among dust-reddened quasars (Urrutia et al. 2009) which are plausibly newly active (e.g., Urrutia et al. 2008). Further, Zhou et al. (2006) identify six BAL RLQs ( $R^* \lesssim 250$  after correcting for intrinsic extinction) with high brightness temperatures suggesting the nucleus is observed from a polar perspective. The presence of BALs in low-inclination RLQs would seem inconsistent with the quasi-equatorial disk-wind model often applied to RQQs.

X-ray observations of BAL RLQs can provide insight into the nature of the BAL outflow, through quantifying any X-ray weakness or spectral hardening associated with BAL-linked absorption. Unfortunately, there have been only a handful of X-ray studies of BAL RLQs to date. Brotherton et al. (2005) conducted a *Chandra* study of five BAL RLQs and found that they were X-ray weak but had relatively soft spectra, consistent with complex absorption or a jet-dominated continuum. These sources were of intermediate radio-loudness (with none having a dereddened  $R^* > 100$ ), and three of the five were in the minority population of low-ionization BAL quasars, which in RQQs display particularly strong X-ray absorption (e.g., Green et al. 2001; Gibson et al. 2009). Wang et al. (2008) present *XMM-Newton* observations of four BAL RLQs believed to be viewed at low inclinations (three of which have low-ionization BALs and only one of which has  $R^* > 100$ ), finding the two detected BAL RLQs to lack intrinsic X-ray absorption and to possess normal X-ray luminosities. X-ray studies of individual BAL RLQs include the work of Schaefer et al. (2006), who find J101614.25+520915.4 to be X-ray weak with significant soft X-ray emission, and Miller et al. (2006), who detect variable X-ray absorption in the BAL RLQ PG 1004+130 (but with an observed column density less than that of most BAL RQQs) and suggest the power-law form and X-ray weakness of the unabsorbed X-ray spectrum may indicate a jet-dominated X-ray nuclear continuum. Statistical efforts to understand the X-ray properties of BAL RLQs require a larger sample covering a wide range of BAL and radio properties.

We here present results from a *Chandra* snapshot survey of a well-defined sample of 12 BAL RLQs primarily selected from the SDSS Data Release 3 (DR3) BAL quasar catalog of Trump et al. (2006). The objects were selected to be distinctly radio-loud ( $R^* \gtrsim 100$ ) with

strong C IV absorption spanning a range of equivalent widths ( $EW^2$ ) and velocities; both core-dominated and lobe-dominated radio sources are included in the sample. For most of these objects we were able to obtain optical spectra and photometry with the Hobby-Eberly Telescope (*HET*) within  $\sim 1$ – $3$  rest-frame weeks of the *Chandra* pointing, to check for BAL and continuum variability. We also make use of *Chandra* archival data for an additional 9 BAL RLQs (including those observed by SDSS in DR4 and DR5), all of which have C IV absorption  $EW > 5 \text{ \AA}$  and  $R^* \gtrsim 50$ . Even taking redshift censoring into account, our sample is dominated by high-ionization BAL quasars, which represent the majority of SDSS-selected BAL quasars (e.g., Trump et al. 2006). We have carefully constructed comparison samples of non-BAL RLQs, BAL RQQs, and non-BAL RQQs observed with SDSS/FIRST/*Chandra* in order to provide proper context for our results and to enable interpretation of the physical nature of BAL outflows in RLQs. Such comparisons are necessitated by the presence of a radio-linked component in the X-ray emission of RLQs, apparent both through increased X-ray luminosity (e.g., Worrall et al. 1987) and X-ray spectral flattening (e.g., Wilkes & Elvis et al. 1987) with increasing radio loudness, and commonly presumed to arise in a small-scale jet.

This paper is organized as follows: §2 describes the selection of the snapshot and archival BAL RLQ samples and the construction of comparison samples, §3 presents the *HET* optical and *Chandra* X-ray observations and provides notes on individual objects, §4 quantifies X-ray luminosities and spectral properties relative to the comparison samples, §5 discusses physical interpretations of BAL RLQs, and §6 summarizes the main conclusions. A standard cosmology with  $H_0 = 70 \text{ km s}^{-1} \text{ Mpc}^{-1}$ ,  $\Omega_M = 0.3$ , and  $\Omega_\Lambda = 0.7$  is assumed throughout. Unless otherwise noted, errors are given as 90% confidence intervals for one parameter of interest ( $\Delta\chi^2 = 2.71$ ). Radio, optical/UV, and X-ray monochromatic luminosities  $l_r$ ,  $l_{uv}$ , and  $l_x$  have units of  $\log \text{ ergs s}^{-1} \text{ Hz}^{-1}$ , at rest-frame frequencies of 5 GHz, 2500  $\text{\AA}$ , and 2 keV, respectively. Object names are typically given as SDSS J2000.

## 2. Sample properties

Our sample of BAL RLQs consists of 21 objects, greatly increasing the number of BAL RLQs with high-quality X-ray coverage. 12 of these BAL RLQs have X-ray data from a *Chandra* snapshot survey (PI Garmire) and 9 have archival *Chandra* coverage. 20/21 BAL RLQs are detected in the 0.5–8 keV band. We also make use of comparison samples of RLQs,

---

<sup>2</sup>We use positive values throughout for C IV absorption EW; emission line properties are not considered in this work. All EW values are rest-frame.

BAL RQQs, and RQQs with *Chandra* coverage.

### 2.1. Selection of snapshot BAL RLQs

The targets for the *Chandra* snapshot survey were selected from the Trump et al. (2006) BAL quasar catalog, which includes SDSS quasars with spectra as of DR3. To ensure consistent consideration of BAL properties, only C IV absorption measurements were used. The Absorption Index (*AI*; Hall et al. 2002) was required to exceed  $1500 \text{ km s}^{-1}$  to remove borderline BALs from further consideration. Note that *AI* is defined from zero velocity with a minimum velocity width of  $1000 \text{ km s}^{-1}$ , and is consequently less restrictive than the traditional Balnicity Index (*BI*; Weymann et al. 1991); several objects in our sample have  $BI = 0 \text{ km s}^{-1}$ . Optical/UV luminosities were determined from SDSS photometry (corrected for Galactic extinction) through redshifting the composite quasar spectrum of Vanden Berk et al. (2001), convolving it with the SDSS filters, and then using the nearest magnitude (or nearest two magnitudes) to  $2500 \times (1+z) \text{ \AA}$  to determine the continuum flux (assuming an optical/UV power-law continuum slope of  $\alpha_\nu = -0.5$ , which is reasonable at these wavelengths). We verified that alternative methods of calculating luminosities (e.g., the spectral-fitting method of Gibson et al. 2009) yield similar results.

These BAL quasars were then checked against the FIRST radio catalog to generate a list of BAL RLQs. Because FIRST has angular resolution sufficient to detect extended radio emission (when present) as distinct sources in many cases, it is necessary to consider the nearby environment to include all components (which could be some combination of core, lobes, and jet) and determine the full radio flux. Candidate matches were considered from all fields in which there was either a FIRST source within  $2''$  of the SDSS optical position, or two or more FIRST sources within  $90''$ . All candidate fields were then examined to exclude intruding background sources (often identifiable due to an optical counterpart seen in the Digitized Sky Survey image). Radio luminosities were calculated at rest-frame 5 GHz, assuming radio power-law continuum slopes of  $\alpha_\nu = -0.5$  for core components and  $\alpha_\nu = -1.0$  for extended components, when present. Candidates for inclusion in the list of *Chandra* snapshot targets were required to be distinctly radio-loud, defined as having  $R^* \gtrsim 100$  and  $l_r > 33$ . The optical spectra were checked for obvious signs of intrinsic reddening (see §2.3) to ensure that the radio-loudness values were not significantly artificially elevated.

The target list for the snapshot *Chandra* survey was then constructed from the brightest (in SDSS  $m_i$ ) BAL RLQs. As can be seen in Figure 1, the survey is substantially complete within DR3 BAL RLQs to  $m_i < 18.6$ . (The single DR3 object near  $m_i = 17.5$  lacking *Chandra* coverage is J144707.41+520340.0, which was considered for inclusion in the target list but

dropped as lowest priority due to having the lowest absorption index,  $AI = 1517 \text{ km s}^{-1}$ .) One BAL RLQ (J112506.95–001647.6) with a fainter  $m_i \simeq 18.9$  was included based on showing extended radio structure. One BAL RLQ (J102258.41+123429.7) with a post-DR3 SDSS spectrum (hence not listed in Trump et al. 2006) was selected from the quasar catalog of Schneider et al. (2007) based on showing extended radio structure along with BAL absorption. The full snapshot sample of BAL RLQs is listed in Table 1.

Gibson et al. (2009) provide an SDSS BAL quasar catalog that covers through DR5, and we make use of this to search for BAL RLQs with archival *Chandra* coverage (see §2.2) and to characterize the BAL properties of the snapshot and archival samples (this catalog was not available at the time of our *Chandra* target selection). All but one (J074610.50+230710.8) of the snapshot BAL RLQs are listed in Gibson et al. (2009), and the listed BAL RLQs targeted in the snapshot survey all have C IV EW  $> 5 \text{ \AA}$ . Since the spectral fitting method and BAL definition in the catalog of Gibson et al. (2009) differ slightly from those used by Trump et al. (2006), minor inconsistencies in absorption properties and object inclusion are to be expected.

## 2.2. Selection of archival BAL RLQs

Two lists of BAL RLQs were checked for archival *Chandra* ACIS non-grating coverage; the first (134 BAL RLQs) was generated by cross-matching quasars with C IV absorption measurements from the BAL catalog of Gibson et al. (2009) with the FIRST catalog, in a manner analogous to that outlined in §2.1, while the second ( $\sim 50$  BAL RLQs) was drawn from mentions of individual BAL RLQs in the literature.<sup>3</sup> Naturally, BAL RLQs can appear in both of these lists. Candidates were required to be definitively radio-loud ( $R^* \gtrsim 50$  and  $l_r > 32$ ) with strong C IV absorption (EW  $> 5 \text{ \AA}$ ). These radio criteria are slightly less stringent than those required of objects in the snapshot BAL RLQ sample, so as to include potentially interesting BAL RLQs with existing X-ray coverage, but still select objects comfortably on the radio-loud side of the canonical  $R^* = 10$  border.

Other X-ray telescopes cannot match the angular resolution of *Chandra*, important for

---

<sup>3</sup>BAL RLQs identified in the following references were checked for archival *Chandra* coverage: Becker et al. 1997; Brotherton et al. 1998; Wills et al. 1999; Gregg et al. 2000; Becker et al. 2000; Becker et al. 2001; Menou et al. 2001; Brotherton et al. 2002; Lacy et al. 2002; Ma et al. 2002; Willott et al. 2002; Jiang & Wang 2003; Benn et al. 2005; Brotherton et al. 2005; Gallagher et al. 2005; Urrutia et al. 2005; Brotherton et al. 2006; Gallagher et al. 2006; Gregg et al. 2006; Miller et al. 2006; Schaefer et al. 2006; Zhou et al. 2006; Just et al. 2007; Kunert-Bajraszewska et al. 2007; Liu et al. 2008; Montenegro-Montes et al. 2008.

minimizing background contamination with faint sources, and many also have lower sensitivities and/or cover a significantly different energy range. We searched the *XMM-Newton* archives for observations pointed to within 15' of any of the BAL RLQs described above, and find coverage of only three objects that would meet our selection criteria: J081102.91+500724.5 (Wang et al. 2008), J101614.25+520915.4 (Schaefer et al. 2006), and J151630.30–005625.5 (PI Boehringer). Adding archival BAL RLQs observed with other X-ray telescopes would not notably increase our sample size or alter our conclusions.

The archival BAL RLQ sample is listed in Table 2. The snapshot and archival BAL RLQs together span a wide range of absorption and radio properties, and constitute a reasonably representative sample of definitively radio-loud BAL RLQs (Figure 2). As mentioned by previous authors (e.g., Shankar 2008), it is rare for quasars to be simultaneously strongly absorbed and strongly radio-loud, but our sample includes a few such objects. The SDSS spectra of the BAL RLQs (Figure 3) display a variety of BAL structures. The majority of the sample BAL RLQs have compact morphologies at arc-second scales, but 4/21 show double-lobed structure and are dominated by extended radio emission.

### 2.3. Reddening

Some BAL RLQs targeted by *Chandra* or mentioned in the literature have unusual and extreme characteristics, and caution is warranted before including such objects in a statistical study. In particular, objects with heavy intrinsic reddening may have artificially elevated apparent radio-loudness values. The BAL RLQs J100424.88+122922.2 (Lacy et al. 2002; Urrutia et al. 2005) and J155633.77+351757.3 (Becker et al. 1997; Brotherton et al. 2005) have radio-loudness values below our selection criteria after correcting for intrinsic reddening (J100424.88+122922.2 is also gravitationally lensed), and are therefore excluded from the archival sample. Both these objects have low-ionization BALs, as do two additional BAL RLQs presented in Brotherton et al. (2005) which are also strongly reddened (such that their corrected radio loudness values are below our selection threshold, although both were already excluded from consideration here due to their low redshifts precluding observation of their C IV absorption properties); this is not unexpected, as low-ionization BAL quasars are known to be generally redder than high-ionization BAL quasars (e.g., Reichard et al. 2003).

We use the relative color indicator  $\Delta(g - i)$  (calculated by subtracting the median quasar color at a given redshift) to check for large intrinsic reddening (e.g., Hall et al. 2006), keeping in mind that RLQs generally show slightly redder colors than do RQQs (e.g., Ivezić et al. 2002). The snapshot and archival BAL RLQs have relative colors that are on average redder than those of SDSS quasars (although most of our BAL RLQs do have relative colors

within the range spanned by 90% of SDSS quasars) but consistent with those of BAL RLQs in general<sup>4</sup> (Figure 4). They do not appear to have strongly distorted radio-loudness values.

The only established low-ionization BAL RLQ in our sample is the archival object J081426.45+364713.5, and although it does have a notably red relative color its  $\Delta(g - i)$  value is within the tail of the BAL RLQ distribution and is significantly less than that of the strongly reddened J155633.77+351757.3 (Figure 4). The CSS BAL RLQ J104834.24+345724.9 suffers from intrinsic reddening (Willott et al. 2002), but its corrected radio-loudness is still quite high, so it is retained in our archival sample but with a dereddened optical luminosity.

## 2.4. Comparison samples

In order to interpret the X-ray properties of BAL RLQs, it is necessary also to analyze comparison samples of non-BAL RLQs (e.g., to gauge the expected X-ray luminosities, including the contribution from an unresolved jet to the X-ray nuclear emission), of BAL RQQs (e.g., to provide context for X-ray absorption relative to UV properties), and of non-BAL RQQs (e.g., to give a baseline for measuring X-ray weakness in BAL RQQs). We caution that the comparison samples we use are specifically chosen to permit comparative investigation of our samples of BAL RLQs and should not necessarily be used to infer general properties of non-BAL RLQs, BAL RQQs, or non-BAL RQQs, particularly those having luminosities outside of the ranges studied here. The optical/UV luminosities and redshifts of the BAL RLQs observed with *Chandra* and of the comparison samples are shown in Figure 5.

We constructed a comparison sample of RLQs by matching the SDSS DR5 Quasar Catalog (Schneider et al. 2007) to FIRST in a manner analogous to that described in §2.1, and then retaining RLQs with *Chandra* coverage with constraints of off-axis angle less than  $12'$ , exposure greater than 1 ks, ACIS-S or ACIS-I used as the detector, and no grating. This list was then filtered to include only RLQs with  $R^* > 50$  and  $l_r > 32$  so as to match the selection criteria for the BAL RLQ archival sample. X-ray luminosities were determined from *Chandra* count rates using the method described in §3.2. There are 68 RLQs selected in this manner, of which 67 (99%) are detected in X-rays. Additional luminous RLQs were added from the sample of Worrall et al. (1987) based on *Einstein* observations; after correcting

---

<sup>4</sup>A Kolmogorov-Smirnov (KS) test comparing the BAL RLQs observed with *Chandra* to SDSS/FIRST BAL RLQs with  $R^* > 50$  and  $EW > 5\text{\AA}$  gives  $p = 0.29$  (comparing to BAL RLQs with  $R^* > 10$  and  $EW > 0\text{\AA}$  gives  $p = 0.12$ ), indicating that the distribution of colors for the snapshot and archival BAL RLQs is not significantly different from that of BAL RLQs in general. Comparing the snapshot and archival BAL RLQs to BAL RQQs gives  $p = 0.03$ .



to our chosen cosmology, we select those RLQs with  $l_{\text{uv}} > 31.3$ , which yields a further 36 RLQs, 32 (89%) with X-ray detections. The total RLQ comparison sample comprises 104 RLQs, 99 (95%) with X-ray detections. Although some of the RLQs have redshifts too low to permit ready observation of the C IV region, the fraction of BAL RLQs is small enough (see references in §1) that any contamination of the comparison sample is minor and does not impact later analysis; we often refer to the RLQ comparison sample as “non-BAL RLQs” throughout.

A comparison sample of BAL RQQs is taken from the BAL catalog of Gibson et al. (2009), combining their Table 1 (absorption properties) with their Table 5 (X-ray data). All high-ionization BAL RQQs with *Chandra* coverage were selected, a total of 37 objects of which 28 (76%) have X-ray detections. We also include those high-ionization BAL RQQs lacking SDSS spectra (i.e., not available for inclusion in the Gibson et al. 2009 catalog) from the Large Bright Quasar Survey (LBQS; e.g., Foltz et al. 1987) observed with *Chandra* by Gallagher et al. (2006), an additional 15 objects, 13 (87%) detected by *Chandra*. The total BAL RQQ comparison sample comprises 52 BAL RQQs, 41 (79%) with X-ray detections.

A comparison sample of non-BAL RQQs is taken from Gibson et al. (2008a); this sample has an excellent combination of size, high-quality X-ray coverage, and well-characterized UV properties. It is composed of the 139 non-BAL RQQs in their sample B, which is made up of optically-selected quasars (SDSS objects targeted exclusively based on FIRST or ROSAT properties excluded) with serendipitous (off-axis angle constrained to be  $1' < \theta < 10'$ ) *Chandra* coverage having exposure  $> 2.5$  ks. These objects span a redshift range of  $1.7 < z < 2.7$ , with the lower-limit set to permit detection of C IV absorption if present (and thereby exclude BAL RQQs) and the upper limit set to permit direct measurement of the 2500 Å continuum flux. We also include 21 highly luminous non-BAL RQQs from Just et al. (2007), taking all objects in their “clean” sample with SDSS and *Chandra* data, to match better the luminosity range of the BAL RLQs. The total RQQ comparison sample comprises 160 RQQs, all of which have X-ray detections.

### 3. Observations and Notes

#### 3.1. HET observations

We obtained optical photometry and spectroscopy of 10/12 of the snapshot BAL RLQs near-contemporaneously with the *Chandra* observations, using the queue-scheduled Hobby-Eberly Telescope (Ramsey et al. 1998). The Low-Resolution Spectrograph (LRS; Hill et al. 1998) was used for the spectroscopic observations, generally with a 1.5" slit and the g2 grating,

providing a resolution of  $R \simeq 867$  (sufficient for productive comparison to SDSS spectra, which have a typical resolution of  $R \simeq 1800$ ). The HET data were reduced with the Image Reduction and Analysis Facility<sup>5</sup> (IRAF) software system using standard techniques, and the resulting spectra are presented in Figure 6. (The *HET* spectrum for J102258.41+123429.7 is not shown; unfortunately the BAL region fell too close to the edge of the chip to provide a useful comparison to the SDSS data.) None of the objects displays strong absorption-line variability, although a few objects show minor changes in BAL structure (see §3.3.1); a more detailed discussion of BAL variability in RLQs is deferred to Miller et al. (in preparation). We also obtained *R*-band images and looked for any flux variability via comparison to field stars and galaxies; none of the observed objects showed large ( $> 0.5$  magnitudes) variability. The *HET* observing log is provided in Table 1.

### 3.2. *Chandra* observations

All snapshot BAL RLQ *Chandra* observations were carried out using the Advanced CCD Imaging Spectrometer (ACIS; Garmire et al. 2003) with exposure times of 4–7 ks. The targets were positioned at the aimpoint of the S3 chip, and data were collected in Very Faint mode. The pipeline processing includes automatic application of both the ACIS charge-transfer inefficiency correction and the time-dependent gain adjustment, and it is carried out using the calibration database version CALDB v3.4.2. The data were analyzed using CIAO version 4.0.2.

The archival BAL RLQ J081426.45+364713.5 has two *Chandra* observations of comparable quality. These were stacked for the purposes of determining source detection and extracting counts, and the resulting increase in signal-to-noise is helpful for more accurately determining the X-ray properties of this faint off-axis source.

Source extraction for the BAL RLQ snapshot and archival objects and for the non-BAL RLQ comparison sample (see §2.2) *Chandra* sources was performed using 90% encircled-energy radii, using nearby source-free regions for background determination. We evaluate source detection through comparison of the observed aperture counts to the 95% confidence upper limit for background alone. Where the number of background counts is less than 10 (as applies in almost all cases) we use the Bayesian formalism of Kraft et al. (1991) to determine the limit; else, we use equation 9 from Gehrels (1986). If the aperture counts exceed the 95% confidence upper limit we consider the source detected and calculate the net counts by subtracting the background from the aperture counts and then dividing by the

---

<sup>5</sup><http://iraf.noao.edu/iraf/web/>

encircled-energy fraction; else, the source is considered undetected and the upper limit is used. All snapshot BAL RLQs are detected, with net 0.5–8 keV counts ranging from 17 to  $\sim 170$  (Table 1), and 8/9 archival BAL RLQs are detected (Table 2). We confirmed source detections for the BAL RLQs by running the CIAO *wavdetect* routine on  $200 \times 200$  square pixel images centered at the SDSS object coordinates, with wavelet scales of 1, 1.41, 2, 2.83, 4, and 5.66 pixels; most sources are detected using a significance threshold of  $10^{-6}$ , while J081426.45+364713.5 is detected (in the stacked image only) using a significance threshold of  $10^{-5}$ .

All BAL RLQs were examined for variability within the *Chandra* observation using the Gregory-Loredo algorithm implemented by CIAO<sup>6</sup>. This method filters by relevant good time intervals and accounts for any dither near chip edges for off-axis sources. The probability that a source is variable can be indicated with a variability index, ranging from 0 to 10; most BAL RLQs had values of 0 (“definitely not variable”) with only 3 objects having variability indices as high as 2 (“probably not variable”). Longer exposures could more tightly constrain variability on ks timescales, while repeat observations could assess variability between epochs.

### 3.3. Notes on individual objects

Optical/UV properties (including absorption characteristics) of the BAL RLQs are listed in Table 3, while radio fluxes and spectral indices are given in Table 4. Below, we briefly comment on interesting aspects of the BAL RLQs.

#### 3.3.1. Snapshot BAL RLQs

*J074610.50+230710.8* has a relatively large C IV absorption index of  $AI = 2955 \text{ km s}^{-1}$  (Trump et al. 2006), and has wide and deep BAL-like absorption structure (Figures 3 and 6) despite being the only snapshot BAL RLQ not included in the Gibson et al. (2009) BAL quasar catalog. The HET spectrum shows enhanced absorption in the higher-velocity BAL (Figure 6), perhaps qualitatively consistent with the tendency of BAL RQQs to vary within narrow discrete regions (Gibson et al. 2008b). It is the reddest snapshot BAL RLQ with  $\Delta(g - i) \simeq 1.1$  (the next reddest snapshot BAL RLQ has  $\Delta(g - i) \simeq 0.6$ ). An archival VLA X-band image (program AB862, observation date 1998-05-04) suggests the radio spectrum of this compact-morphology source peaks near 5 GHz.

---

<sup>6</sup><http://cxc.harvard.edu/ciao/ahelp/glvary.html>

*J083749.59+364145.4* has particularly strong C IV, Si IV, Ly  $\alpha$ , and O VI BALs. The C IV EW of 34.6 Å is the largest in the snapshot or archival BAL RLQ sample. It appears to have a GHz-peaked (possibly variable) radio spectral shape and is unresolved at milliarcsecond scales (Montenegro-Montes et al. 2008, 2009).

*J085641.58+424254.1* displays strong N V absorption. The HET spectrum suggests the C IV emission line might be slightly variable.

*J092913.96+375742.9* (also FBQS J092913.9+375742) appears to be resolved in an X-band VLA image (program AG0574, observation date 1999-07-12). There is a jet-like feature with a flux of 2.1 mJy located 0.5" West of the core.

*J102258.41+123429.7* is resolved into a double-lobed morphology by FIRST (see Figure 7), and the southern lobe shows extended diffuse emission past the primary hotspot. The *Chandra* image does not show any extended X-ray emission, but there are only  $\sim 20$  X-ray source counts.

*J105416.51+512326.0* has a flat radio spectrum that steepens to  $\alpha_r = -0.35$  above 1.4 GHz.

*J112506.95–001647.6* is resolved into a double-lobed morphology by FIRST (de Vries et al. 2006; see Figure 7). The *Chandra* image does not show any extended X-ray emission; there are  $\sim 80$  X-ray source counts. The primary C IV absorption trough is at low velocity and splits the emission line.

*J115944.82+011206.9* (also B1157+014) was identified as a BAL RLQ by Menou et al. (2001), who noted that in addition to the primary low-velocity BAL there is an additional absorption trough near 8000 km s $^{-1}$ . The depth of this secondary absorption may have increased slightly between the SDSS and HET observations. The radio spectrum appears to be double-peaked (Montenegro-Montes et al. 2008). The source shows symmetric jet-like extended emission on milliarcsecond scales and a one-sided misaligned sequence of faint knots stretching to  $\sim 100$  milliarcseconds (Montenegro-Montes et al. 2009). *J115944.82+011206.9* has the lowest  $m_i$  in the snapshot sample and has sufficient X-ray counts ( $\sim 170$  from 0.5–8 keV) for basic spectral analysis (Figure 8). The relatively hard X-ray spectrum suggests intrinsic absorption; a neutral absorber has a best-fit column density of  $N_H = 3.2_{-2.1}^{+2.9} \times 10^{22}$  cm $^{-2}$  with an unusual flat photon index of  $\Gamma = 1.06_{-0.33}^{+0.35}$  required.

*J123411.73+615832.6* has an atypical BAL structure, with a deep and wide trough that decreases gradually in depth until smoothly meeting the base of the Si IV emission line. Narrow redshifted C IV absorption is also present. A C-band VLA image (program AP450, observation date 2003-02-27) indicates the radio spectral index is  $\alpha_r \simeq -0.5$ .

*J133701.39–024630.3* has the highest measured X-ray hardness ratio in the snapshot or archival BAL RLQ sample. A C-band VLA image (program AG400, observation date 1994-01-08) suggests this is a flat-spectrum RLQ with  $\alpha_r \simeq -0.1$ .

*J141334.38+421201.7* (also FBQS J141334.4+421201) was identified as a BAL RLQ by Becker et al. (2000). The radio spectrum is complex (Montenegro-Montes et al. 2008) while the morphology is compact with a one-sided jet on milliarcsecond scales (Liu et al. 2008).

*J162453.47+375806.6* is described in detail by Benn et al. (2005), and we use their value of  $BI = 2990 \text{ km s}^{-1}$  and estimate  $V_{\text{max}} = 28300 \text{ km s}^{-1}$  rather than taking measurements from Gibson et al. (2009) (for which BAL absorption was integrated to  $25000 \text{ km s}^{-1}$ ). The large minimum ( $V_{\text{min}} = 20560 \text{ km s}^{-1}$ ) and maximum velocities of the C IV BAL in this source are unusual for BAL RLQs and unique within our snapshot and archival samples. There is also low-velocity absorption, described by Benn et al. (2005) as a mini-BAL (defined as total velocity range  $< 2000 \text{ km s}^{-1}$ ; the mini-BAL is shaded gray along with the primary BAL in Figure 6 for identification). The radio spectrum is GHz-peaked (steep at high frequencies) and milliarcsecond imaging reveals a one-sided jet (Benn et al. 2005; Montenegro-Montes et al. 2008, 2009).

### 3.3.2. Archival BAL RLQs

*J020022.01–084512.0* (also FBQS J0200–0845) was identified as a BAL RLQ by Becker et al. (2001). It was observed serendipitously in an  $\sim 18$  ks ACIS-I image (ObsID 3265; PI Ebeling) and is discussed by Gallagher et al. (2005). The source has a radio-loudness value of  $R^* = 48$ , on the border for inclusion in the archival sample.

*FBQS J0256–0119* was identified as a BAL RLQ by Becker et al. (2001). Flux measurements by Montenegro-Montes et al. (2008) indicate a steep radio spectrum; those authors also note the increased flux measured by FIRST relative to NVSS may be due to variability. The  $\sim 5$  ks ACIS-S observation shows FBQS J0256–0119 to be X-ray weak but with a soft spectrum (Brotherton et al. 2005). We do not have access to photometric magnitudes for this object, so we take the lack of intrinsic reddening noted by Brotherton et al. (2005) as justification to set the relative color  $\Delta(g - i) = 0$ .

*J081426.45+364713.5* has a low radio luminosity ( $l_r = 32.7$ ) and the reddest relative color [ $\Delta(g - i) = 1.1$ ] in the snapshot or archival BAL RLQ sample. The optical spectrum shows deep and wide BALs in both high and low-ionization lines (Trump et al. 2006 categorize it as an FeLoBAL) and only weak emission lines. It was observed serendipitously in two  $\sim 10$  ks ACIS-I exposures (ObsID 3436, 3437; PI Fox) and is X-ray weak.

*J091951.29+005854.9* has a non-zero  $BI = 673.1 \text{ km s}^{-1}$  and a C IV EW of  $6.9 \text{ \AA}$ , but the BAL is relatively narrow and the absorption index is low ( $AI = 1268 \text{ km s}^{-1}$ ). The radio loudness is also borderline for our sample ( $R^* = 51$ ). It was observed serendipitously in a  $\sim 5$  ks ACIS-S image (ObsID 7056; PI Murray) but is not detected.

*J100726.10+124856.2* (also PG 1004+130) is a low-redshift ( $z = 0.24$ ) RLQ in which BALs were discovered by Wills et al. (1999); we use their values of  $BI = 850 \text{ km s}^{-1}$  and  $V_{\text{max}} = 10000 \text{ km s}^{-1}$  since the SDSS spectrum does not cover the C IV region. It is also a hybrid-morphology radio source (Gopal-Krishna & Wiita 2000), with an edge-brightened lobe opposite a broadening edge-darkened jet. It is perhaps the best-studied BAL RLQ at X-ray frequencies: deep *XMM-Newton* and *Chandra* observations show X-ray absorption variability and also reveal X-ray jet emission (Miller et al. 2006). PG 1004+130 is X-ray weak relative to comparable non-BAL RLQs.

*J104834.24+345724.9* (also 4C +35.23) is a CSS RLQ with a C IV BAL identified by Willott et al. (2002). It is radio luminous, and even after correcting for some intrinsic reddening it remains notably radio-loud (Kunert-Bajraszewska et al. 2007). It was targeted by *Chandra* in a  $\sim 5$  ks ACIS-S observation (ObsID 9320; PI Kunert-Bajraszewska) and is detected with a hard X-ray spectral shape.

*J122033.87+334312.0* (also 3C 270.1) is a double-lobed steep-spectrum RLQ with the second-highest radio-loudness ( $\log R^* = 4.2$ ) in the snapshot or archival BAL RLQ sample. Low-velocity C IV absorption has been known to be present in this object for some time (e.g., Anderson et al. 1987) although it has not necessarily been described as a BAL quasar; however, the balnicity index measured from the SDSS data is non-zero ( $BI = 52.5$ ; Gibson et al. 2009). J122033.87+334312.0 was observed serendipitously in a  $\sim 3$  ks ACIS-S exposure (ObsID 2118; PI Cagnoni).

*J131213.57+231958.6* (also FBQS J131213.5+231958) was identified as a BAL RLQ by Becker et al. (2000) and shows a wide and deep C IV absorption trough that extends to  $25000 \text{ km s}^{-1}$  (from FBQS data; the DR7 SDSS spectrum does not have sufficient short wavelength coverage to see the BAL). It shows two-sided extended radio emission on milliarcsecond scales but is core dominated (Jiang et al. 2003) and likely variable (Montenegro-Montes et al. 2008); these radio characteristics do not provide a self-consistent orientation measure. Liu et al. (2008) suggest this object is similar in some respects to CSS sources. The  $\sim 5$  ks ACIS-S observation (Brotherton et al. 2005) shows it to be X-ray weak but with an X-ray spectrum actually somewhat softer than is typical of non-BAL RLQs.

*LBQS 2211–1915* was identified as a “marginal” BAL quasar by Weymann et al. (1991), with a non-zero but low  $BI = 27 \text{ km s}^{-1}$ , and is radio-loud based on an NVSS flux mea-

surement. The  $\sim 6$  ks ACIS-S observation (Gallagher et al. 2006) shows it to be X-ray weak relative to non-BAL RLQs. We estimate the relative color to be  $\Delta(g - i) = 0.32$  based on data from Gallagher et al. (2007).

## 4. Data Analysis

Because RLQs are generally more X-ray luminous than comparable RQQs (e.g., Worrall et al. 1987), a direct comparison of the X-ray properties of BAL RLQs to those of BAL RQQs is of limited value. To gain additional insight, we quantify the degree to which BAL RLQs are X-ray weak relative to non-BAL RLQs, then compare this to the X-ray decrement for BAL RQQs relative to non-BAL RQQs. Much of the X-ray weakness of BAL RQQs may be explained by low-energy X-ray absorption (e.g., Gallagher et al. 2006), which can produce X-ray spectra that are harder than typical; examination of the X-ray spectral properties of BAL RLQs compared with those of non-BAL RLQs can clarify whether a similar effect typically applies to BAL RLQs.

### 4.1. Calculation of X-ray hardness ratios and luminosities

When insufficient counts are available for productive spectral modeling, as is unfortunately the case for the majority of our data, the relative contributions of hard and soft X-ray emission to the overall spectrum can be assessed from the hardness ratio  $HR = (H - S)/(H + S)$ , where  $H$  and  $S$  are the net hard-band (2–8 keV) and soft-band (0.5–2 keV) counts, respectively. Large values of the hardness ratio can indicate intrinsic absorption, or alternatively an unusually flat power-law (or both effects together). Since all our data are taken from *Chandra* (including the non-BAL RLQ, BAL RQQ, and non-BAL RQQ comparison samples) we can compare hardness ratios without concern for instrumental cross-calibration effects. Hardness ratios for objects observed with one of the front-illuminated CCDs have been adjusted by subtracting 0.14 to enable direct comparison to the hardness ratios for the back-illuminated CCDs (such as S3, which covers the ACIS-S aimpoint).

The probability distribution for the hardness ratio can be calculated using the Bayesian formalism detailed in Jin et al. (2006), using a uniform prior (i.e., their equation 13). The maximum-likelihood hardness ratio is simply  $(H - S)/(H + S)$ . We use this method to calculate  $1\sigma$  errors on the value of  $HR$ , defined such that 68% of the area above (below) the maximum likelihood hardness ratio is enclosed within the range of the upper (lower) bound (e.g., Wu et al. 2007). Where the total number of counts exceeds 100 symmetric errors are

calculated from equation 8 of Jin et al. (2006).

X-ray luminosities are calculated from the 0.5–8 keV count rates, which are converted to observed-frame 2 keV flux densities with PIMMS<sup>7</sup>, in all cases assuming Galactic absorption and a power-law spectrum with  $\Gamma=1.5$ . This model is typical of RLQs: for example, Reeves & Turner (2000) found  $\langle\Gamma\rangle = 1.66$  with  $\sigma = 0.22$  for an *ASCA* sample of 35 RLQs, while Page et al. (2005) determined  $\langle\Gamma\rangle = 1.55$  with  $\sigma = 0.29$  for an *XMM-Newton* sample of 16 RLQs at  $z > 2$ . However, reasonable alternate choices for  $\Gamma$  have only a few percent impact upon the calculated X-ray fluxes. Count rates for archival observations were converted to flux densities using the calibration appropriate to that cycle, in order to account for the temporal changes in ACIS sensitivity. The ACIS-I model in PIMMS was used for all front-illuminated chips.

The bandpass-corrected X-ray luminosities  $l_x$  are given in units of  $\log \text{ ergs s}^{-1} \text{ Hz}^{-1}$  at rest-frame 2 keV in Table 5. We also calculate X-ray luminosities  $l_{x,S}$  and  $l_{x,H}$  at rest-frame 2 keV determined from the soft and hard-band count rates, respectively, in order to investigate the influence of spectral shape (and intrinsic absorption) on the X-ray luminosity.

#### 4.2. Relative X-ray luminosities

X-ray and optical/UV luminosities are correlated in quasars, and so to evaluate the degree of X-ray weakness in BAL quasars it is necessary to compare to non-BAL quasars of similar optical/UV luminosity. Extensive studies (e.g., Avni & Tananbaum 1986; Strateva et al. 2005; Steffen et al. 2006; Just et al. 2007; Kelly et al. 2007) have demonstrated that X-ray luminosity in non-BAL RQQs may be parameterized as  $l_x \propto \beta \times l_{uv}$ , where  $\beta \simeq 0.6 - 0.8$  (i.e., the linear ratio of monochromatic optical/UV luminosity to monochromatic X-ray luminosity increases with increasing  $l_{uv}$ ). There is continuing debate (e.g., Just et al. 2007; Kelly et al. 2007) as to whether the optical/UV-to-X-ray properties of individual RQQs are also significantly dependent upon redshift, but for our purposes the  $l_x(l_{uv})$  parameterization is fully satisfactory to explore the large deviations from predicted X-ray luminosity that are seen in BAL quasars. We make use of the relation  $l_x = 0.636 \times l_{uv} + 7.055$  (a linear fit to  $\log$  luminosities) found by Just et al. (2007) taking  $l_x$  as the dependent variable and fitting their large sample of non-BAL RQQs using the Astronomy Survival Analysis Package (ASURV; Lavalley et al. 1992). Using the Bayesian maximum-likelihood method of Kelly (2007), which accounts for both upper limits and errors (we presume uncertainties are dominated by typical quasar variability; cf. §3.5 of Gibson et al. 2008), and fitting our comparison sample of RQQs

---

<sup>7</sup><http://cxc.harvard.edu/toolkit/pimms.jsp>



yields a similar relation<sup>8</sup> of  $l_x = (0.574 \pm 0.057) \times l_{uv} + (8.995 \pm 1.772)$ .

As an initial step toward understanding the X-ray luminosities of BAL RLQs, we fit  $l_x(l_{uv})$  for non-BAL RLQs as for non-BAL RQQs, finding a best-fit correlation of  $l_x = (0.905 \pm 0.079) \times l_{uv} - (0.813 \pm 2.459)$ , with significant scatter (Figure 9a). The majority of snapshot and archival BAL RLQs have X-ray luminosities less than those of non-BAL RLQs with comparable optical/UV luminosities, typically by a factor of 4.1–8.5 (median 6.6). However, the difference between observed and predicted X-ray luminosity in BAL RLQs is not as extreme as that for BAL RQQs relative to non-BAL RQQs (Figure 9b); here the difference is typically a factor of 2.8–34.0 (median 11.4) but exceeds 40 for  $\simeq 15\%$  of BAL RQQs. The sample BAL RLQs also tend to be X-ray weaker than non-BAL RQQs at low optical/UV luminosities.

The X-ray luminosities of non-BAL RLQs can also be parameterized as a function of radio luminosity, with a best-fit result for the comparison non-BAL RLQ sample of  $l_x = (0.617 \pm 0.043) \times l_r + (6.328 \pm 1.480)$  (Figure 9c). Some BAL RLQs again tend to fall below the non-BAL RLQ correlation, although to a lesser degree, while some are matched in radio and X-ray properties to comparable non-BAL RLQs. Possibly the reduced offset in  $l_x(l_r)$  for BAL RLQs reflects not only X-ray weakness but also lower radio-loudness values for BAL RLQs than for the comparison non-BAL RLQs; the median value of  $\log R^*$  is 2.2 for the BAL RLQs and 3.0 for the RLQs. The outlier with high radio luminosity and low X-ray luminosity is the CSS source J104834.24+345724.9 (see also §5.2). Fitting X-ray luminosity as a joint function of optical/UV *and* radio luminosity yields a relation with reduced scatter:  $l_x = (0.472 \pm 0.085) \times l_{uv} + (0.413 \pm 0.054) \times l_r - (1.392 \pm 1.192)$  (Figure 9d). Due to the similar coefficients BAL RLQs have essentially averaged offsets from  $l_x(l_{uv})$  and  $l_x(l_r)$  for  $l_x(l_{uv}, l_r)$ . Obviously more sophisticated models are possible, but this provides a useful quantitative measure of X-ray luminosity in BAL RLQs relative to RLQs taking into account both optical/UV and radio properties.

The difference between the observed X-ray luminosity in BAL RLQs and that predicted from non-BAL RLQs with comparable optical/UV luminosities,  $\Delta l_{x,uv} = l_x - l_x(l_{uv})$ , is plotted as a histogram in Figure 10a. The scatter for non-BAL RLQs (Figure 10b) is smaller than the degree to which BAL RLQs are X-ray weak. However, BAL RLQs do not extend to extreme values of X-ray weakness (log offsets of  $< -1$ ), as do some BAL RQQs (Figure 10c; here  $\Delta l_{x,uv}$  is calculated from the Just et al. 2007 relation for non-BAL RQQs) relative to non-BAL RQQs (Figure 10d). Note that the underlying distribution of  $\Delta l_{x,uv}$  for BAL

---

<sup>8</sup>Here and for subsequent model fits the quoted parameter values are the median of draws from the posterior distribution and the errors are  $1\sigma$ .

RQQs is even X-ray weaker than the histogram in Figure 10c suggests, as there are a large number of X-ray upper limits. There appears to be a limit to how X-ray weak BAL RLQs can become. The Kaplan-Meier estimates of the median  $\Delta l_{x,uv}$  values are  $-0.82$ ,  $-0.03$ , and  $-1.06$  for BAL RLQs, non-BAL RLQs, and BAL RQQs, respectively. A Peto-Prentice two-sample test indicates that the distribution of  $\Delta l_{x,uv}$  values for BAL RLQs is significantly different from that of non-BAL RLQs (test statistic 6.621,  $p < 5 \times 10^{-5}$ ) and BAL RQQs (test statistic 2.249,  $p = 0.02$ ). Figure 10e shows a histogram of the difference between the observed X-ray luminosity in BAL RLQs and that predicted from non-BAL RLQs with comparable optical/UV *and* radio luminosities,  $\Delta l_x = l_x - l_x(l_{uv}, l_r)$ . BAL RLQs are a factor of 2.0–4.5 (median 3.2) weaker in X-rays than comparable non-BAL RLQs. The results are similar if the relative X-ray luminosity is instead calculated from the soft or hard-band luminosities,  $l_{x,S}$  and  $l_{x,H}$  (Figures 10f and 10g).

There is a general trend in quasars relating C IV absorption to X-ray weakness (e.g., Brandt, Laor, & Wills 2000; Laor & Brandt 2002; Gallagher et al. 2006). We plot the relative X-ray luminosity for BAL RLQs [presented as  $\Delta\alpha_{ox}$  for ease of comparison to previous work, where  $\alpha_{ox} = 0.384 \times (l_x - l_{uv})$  and  $\Delta\alpha_{ox} = \alpha_{ox} - \alpha_{ox}(l_{uv})$  with  $\alpha_{ox}(l_{uv})$  calculated from the  $l_x(l_{uv})$  relations given above] versus C IV EW (Figure 11a) and maximum outflow velocity (Figure 11b). It is apparent that even BAL RLQs with large C IV equivalent widths (10–40 Å) do not have  $\Delta\alpha_{ox} < -0.5$ , as do many strongly absorbed BAL RQQs. BAL RLQs appear to follow the correlation between maximum outflow velocity and relative X-ray luminosity that holds for BAL RQQs, but only to a limiting value of  $\Delta\alpha_{ox}$ , near which BAL RLQs are observed with a wide range of outflow velocities.

Additional context for interpreting the relative X-ray luminosities of some BAL RLQs is provided by their radio morphologies or spectral properties, which can constrain source inclination (e.g., Wills & Brotherton 1995) or age (e.g., Stawarz et al. 2008). Lobe-dominated BAL RLQs (nested symbols in Figures 9 and 11), which presumably lie at larger angles to the line of sight than do core-dominated BAL RLQs, show a range of behavior: J112506.95–001647.6 and J122033.87+334312.0 are actually X-ray bright relative to non-BAL RLQs with similar optical/UV luminosities, whereas J102258.41+123429.7 and particularly J100726.10+124856.2 (PG 1004+130) are X-ray weak. J122033.87+334312.0 becomes X-ray weak when radio luminosity is also taken into account, and perhaps the X-ray brightness of J112506.95–001647.6 reflects its relatively weak C IV BAL (low absorption index and maximum velocity). Plausibly young objects [including the GPS sources J083749.59+364145.4 and J162453.47+375806.6, and the CSS source J104834.24+345724.9 (4C+35.23)] seem to have strong BALs and to be X-ray weak, but additional data are required to investigate such trends in detail.

### 4.3. X-ray spectral characteristics

Most of the quasars in the snapshot and archival BAL RLQ samples and in the non-BAL RLQ, BAL RQQ, and non-BAL RQQ comparison samples lack sufficient counts for productive spectral fitting, so we investigate basic X-ray spectral properties using hardness ratios (see §4.1). We are primarily interested in whether BAL RLQs show evidence for intrinsic X-ray absorption. Absorption by a neutral column will preferentially remove soft X-ray emission and lead to greater values of  $HR$ , although this effect can be diluted by complex (partial covering or ionized) absorption, such as is established to occur in BAL RQQs (e.g., Gallagher et al. 2002, 2006) and has been suggested for BAL RLQs (e.g., Brotherton et al. 2005). Absorption spectral effects are also diluted by increasing redshift pushing the rest-frame soft band to lower observed-frame energies.

The non-BAL RLQs in our comparison sample have relatively uniform hardness ratios that do not appear strongly dependent upon redshift (Figure 12a), suggesting that the spectra for these RLQs are generally dominated by a simple power-law component with a standard photon index and insignificant intrinsic absorption. Many BAL RLQs have hardness ratios similar to those of non-BAL RLQs, but there are several BAL RLQs with harder X-ray spectra, although none with measured  $HR > 0.2$ . A Peto-Prentice two-sample test indicates that the distribution of  $HR$  values for BAL RLQs is significantly different from that of non-BAL RLQs (test statistic 3.704,  $p = 2 \times 10^{-4}$ ). BAL RQQs typically have harder X-ray spectra than non-BAL RQQs (the distributions are statistically different, with  $p < 5 \times 10^{-5}$ ) and can have extreme hardness ratios (Figure 12b). The distribution of hardness ratios for the snapshot and archival sample of BAL RLQs is not statistically inconsistent with that of BAL RQQs (test statistic 1.396,  $p = 0.16$ ). The Kaplan-Meier estimates of the median/mean  $HR$  values for the BAL RLQs, non-BAL RLQs, BAL RQQs, and non-BAL RQQs in our samples are  $-0.40$ ,  $-0.52$ ,  $-0.26$ , and  $-0.57$ , respectively; the distribution for BAL RLQs is skewed, with a Kaplan-Meier estimate of the mean  $HR$  of  $-0.34$ . The slightly higher median  $HR$  for non-BAL RLQs relative to non-BAL RQQs might be expected from prior X-ray spectral studies, but the distributions for our comparison samples of non-BAL RLQs and non-BAL RQQs are not statistically inconsistent ( $p = 0.23$ ; possibly the more radio-luminous RLQs observed by *Einstein* would have slightly larger *Chandra* hardness ratios than the RLQs plotted here). For reference, a photon index of  $\Gamma = 2$  approximately corresponds to  $HR = -0.6$  and  $\Gamma = 1.7$  to  $HR = -0.5$ .

Five BAL RLQs have particularly hard X-ray spectral shapes (with  $HR > -0.2$ ) relative to both RLQs and other BAL RLQs; these objects include J092913.96+375742.9 and J115944.82+011206.9 (both of which apparently have small-scale radio jet emission), J133701.39–024630.3, J100726.10+124856.2 (PG 1004+130, for which the *XMM-Newton*

spectrum is softer), and J104834.24+345724.9 (the CSS source 4C+35.23). Although this study is not designed to investigate the X-ray spectral properties of various subcategories of BAL RLQs, we note briefly that the GPS sources J083749.59+364145.4 and J162453.47+375806.6 have soft X-ray spectral shapes, and the FeLoBAL J081426.45+364713.5 has an intermediate  $HR = -0.29$ , slightly harder than the median for the BAL RLQs studied here.

The correlation between X-ray weakness and hardness ratio in BAL RQQs (Figure 12d) is reflective of (often complex) absorption reducing the soft-band X-ray flux in BAL RQQs (e.g., Gallagher et al. 2006). A similar trend is not obviously apparent for BAL RLQs (Figure 12c), for which there are several X-ray weak objects with low hardness ratios (or soft X-ray spectra), and essentially no BAL RLQs with  $\Delta l_x(l_{uv}) \lesssim -1$ . Note that our observations are sensitive to low values of  $\Delta l_x(l_{uv})$  (only one undetected BAL RLQ is not plotted, and many of the rest could be detected if they were even X-ray weaker by a linear factor of 5–10; see net counts in Tables 1 and 2); the sample simply lacks notably X-ray weak BAL RLQs. It does not appear possible to ascribe X-ray weakness in BAL RLQs to intrinsic absorption (with properties as in BAL RQQs) obscuring the *entire* nuclear X-ray continuum source, although such an interpretation could hold for some particular BAL RLQs.

## 5. Discussion

### 5.1. Physical models

The above results suggest a picture in which BAL RLQs are in some sense intermediate between BAL RQQs and non-BAL RLQs: BAL RLQs are X-ray weak, but not to the same relative degree as are BAL RQQs, and they can have harder X-ray spectra, but often have hardness ratios consistent with those of non-BAL RLQs. A simple physical model could also portray BAL RLQs as having X-ray characteristics of both BAL RQQs (an outflowing BAL wind that is associated with an X-ray absorber) and non-BAL RLQs (an unresolved X-ray emitting jet that contributes to the total continuum). There are too many free parameters to constrain such a model in detail, but some insight can be gained by making the simplifying assumptions that the disk-corona emission in RLQs has the same optical/UV-to-X-ray properties as are observed in RQQs [i.e., that any systematic differences in the accretion structure of RLQs compared to RQQs do not produce dramatic changes in the  $l_x(l_{uv})$  relation], and that the optical luminosity in RLQs is dominated by disk-related emission with only a minimal jet-linked contribution (certainly plausible for these broad-line RLQs, and often inferred for even RLQs in which the radio and X-ray emission is established as jet-dominated; e.g., Sambruna et al. 2006). Then the disk-corona X-ray luminosity in RLQs may be calculated using the  $l_x(l_{uv})$  relation for RQQs, and any additional X-ray luminosity may be ascribed to

jet-linked emission.

The ratio of total RLQ X-ray luminosity to equivalent RQQ (disk-corona) X-ray luminosity increases with increasing radio luminosity (Figure 13a); this presumably reflects increasing jet luminosity at both radio and X-ray frequencies with decreasing inclination. The precise nature of the X-ray jet emission in RLQs (and its dependence upon inclination) remains a matter of debate, although it seems likely that two-zone models are required (e.g., Jester et al. 2006), in which beamed jet-linked X-ray emission from the fast spine dominates for objects viewed at low inclinations while a slower (and less beamed) sheath could generate jet-linked X-ray emission radiated in a more isotropic manner. We refrain from imposing a particular jet model upon the data but quantify the observed increase in the X-ray luminosity of RLQs relative to RQQs with increasing radio luminosity through the trendline shown in Figure 13a. Non-BAL RLQs with optical/UV and radio luminosities similar to those of the BAL RLQs in our sample would have total X-ray luminosities greater than the non-BAL RQQ equivalent by a typical multiplicative factor of 1.8–2.7, suggesting roughly equal contributions from disk-corona and jet-linked X-ray emission.

If we further presume that the X-ray absorber in BAL RLQs has characteristics similar to those found for BAL RQQs, then based on Figure 10c the disk-corona emission ought to be reduced by a factor of  $\sim 10$  in BAL RLQs relative to non-BAL RLQs. If the jet-linked X-ray emission were also absorbed to a similar degree, the entire X-ray continuum in BAL RLQs would be veiled as in BAL RQQs and the relative X-ray luminosities and hardness ratios of BAL RLQs would agree better with those of BAL RQQs, contrary to observation. However, it seems that the jet must be partially covered by the BAL-linked X-ray absorber in order to explain the difference between predicted and observed jet-linked X-ray emission in BAL RLQs. Specifically, we find that many BAL RLQs have jet-linked X-ray emission only 20–80% of that expected, and further those BAL RLQs with hardness ratios harder than 90% of RLQs tend to have less jet-linked X-ray emission than predicted (Figure 13b). We postulate that the BAL-linked X-ray absorber is of sufficient size to cover some fraction of the X-ray emitting jet in many BAL RLQs.

Alternative scenarios are possible; while we cannot rule them out, they are difficult to motivate either physically or from the data. It might be surmised that BAL RLQs are intrinsically X-ray weak relative to RLQs and are also (typically) unabsorbed. The X-ray absorber is thought to shield the BAL wind from overionization in disk-wind models (e.g., Murray et al. 1995), so such a postulated lack of an X-ray absorber could require BAL formation and acceleration to occur in a manner distinct from that in BAL RQQs. One mechanism by which BAL RLQs could be intrinsically X-ray weak would be if the presence of a BAL outflow inhibited the production of small-scale jet-linked X-ray emission.

If the disk/corona system were relatively similar to that of RQQs, then BAL RLQs should follow the non-BAL RQQ luminosity correlations; however, BAL RLQs with lower radio luminosities have X-ray luminosities less than those of non-BAL RQQs with comparable optical/UV luminosities (Figures 9a and 13a). Another mechanism by which BAL RLQs could be intrinsically X-ray weak would be for the disk/corona system to be an inefficient emitter of X-rays. If the small-scale X-ray emitting jet were relatively similar to that in RLQs, then as the fractional contribution in RLQs from the disk/corona would be expected to decrease at high radio luminosities, the difference in X-ray luminosity between BAL RLQs and RLQs should likewise decrease; however, the offset between BAL RLQs and RLQs appears roughly constant (Figures 9c and 9d) across the two orders of magnitude in radio luminosity spanned by our sample. In any event, it seems most straight-forward to retain those fundamental features firmly established as present in BAL RQQs or RLQs when interpreting BAL RLQs, and the simple model associated with Figure 13 and described above suffices to explain the current data naturally.

## 5.2. BAL RLQ geometries and ages

There have been suggestions that BAL outflows occur at low inclinations (e.g., Brotherton et al. 2006; Zhou et al. 2006), something difficult to explain from simple disk-wind models. Some of the BAL RLQs in our sample have radio properties consistent with the jet being pointed close to the line of sight, including compact morphologies and flat radio spectra, although GPS sources with sparsely sampled radio spectra can mimic such characteristics at a range of inclinations. It does not seem likely that outflows in BAL RLQs must always be polar, since some of the BAL RLQs in our sample are steep-spectrum objects dominated by extended radio emission, arguing against low inclinations for these objects. We can estimate the inclinations of the core-dominated BAL RLQs using the core-radio-to-optical luminosity ratio (essentially the radio loudness, excluding lobe emission; Wills & Brotherton 1995), and find probable inclinations of  $\sim 20^\circ$  to  $> 40^\circ$ , but this method is insensitive to larger inclinations and may not apply to BAL RLQs. The sample BAL RLQs do not tend to have large values of  $R^*$  ( $\gtrsim 500$ – $1000$ ), with the two exceptions being a lobe-dominated and a CSS RLQ, suggesting most are not low inclination sources (cf. Figure 1 of Wills & Brotherton 1995).

The discovery of BALs in RLQs which are compact and have radio spectra similar to those of presumed young GPS or CSS sources has led to suggestions that BALs are associated

with a quasar evolutionary phase.<sup>9</sup> Not all GPS or CSS sources display BALs, and not all BAL RLQs are associated with young sources;<sup>10</sup> if there is no inclination dependence to BALs then (as assessed by Shankar et al. 2008) strictly evolutionary models require problematic fine tuning of the various phases to match observations. It is possible to compare directly the X-ray properties of GPS and CSS sources to those of BAL RLQs to search for similarities. We plot data from *Chandra* observations of GPS and CSS radio galaxies and RLQs carried out by Siemiginowska et al. (2008) on the  $l_x(l_{uv})$  and  $l_x(l_r)$  relations shown earlier (Figure 14). GPS/CSS sources are often X-ray weak relative to RLQs of similar optical/UV luminosity, but they are also often extremely radio-loud (see also the spectral energy distribution plots from Siemiginowska et al. 2008) in a manner that the (non-GPS, non-CSS) BAL RLQs are not. The CSS BAL RLQ J104834.24+345724.9 is both radio luminous and X-ray weak, with a hard X-ray spectrum atypical of GPS/CSS sources, as might be expected for an object in both classes.

## 6. Conclusions

This work presents and discusses the X-ray properties of 21 BAL RLQs observed with *Chandra*. The sample of BAL RLQs spans a wide range of C IV absorption properties, is dominated by high-ionization BAL quasars, is restricted to definitively radio-loud quasars with  $R^* \gtrsim 50$ , and includes objects with both core-dominated and lobe-dominated radio morphologies. We find the following results:

1. BAL RLQs are X-ray weak relative to non-BAL RLQs of similar optical/UV luminosity, but not to as extreme a degree as are BAL RQQs relative to comparable non-BAL RQQs. BAL RLQs are also X-ray weak, to a lesser extent, relative to non-BAL RLQs of similar radio luminosity or of both similar optical/UV and radio luminosities.

2. BAL RLQs do not show a strong correlation between X-ray spectral hardness and X-ray weakness, as is observed in BAL RQQs, and do not tend to have as extreme hardness ratios as can BAL RQQs.

3. The simplest model to explain our results is that the X-ray continuum in BAL RLQs consists of both disk/corona and jet-linked X-ray emission; absorption of the disk/corona

---

<sup>9</sup>The relatively high fraction of low-ionization BAL quasars among dust-reddened quasars has also motivated the association of (at least low-ionization) BALs with young quasars (e.g., Urrutia et al. 2009).

<sup>10</sup>As in our sample, BAL RLQs can be found in FR IIs with large projected sizes, although the rarity of such objects is interpreted by Gregg et al. (2006) as support for an evolutionary scenario.

emission alone typically will neither reduce the observed X-ray luminosity nor harden the X-ray spectrum of BAL RLQs to the same degree as in BAL RQQs.

4. Although jet-linked X-ray emission in BAL RLQs does not generally appear to be absorbed to the same degree as is the X-ray continuum in BAL RQQs, it does seem likely that the X-ray emitting small-scale jet is partially covered in many BAL RLQs.

Microquasar observations have been interpreted to show that in the soft state a radiatively-driven disk wind develops and becomes the dominant channel for outflow of accreting material, quenching the jet (Neilsen & Lee 2009). Although the dearth of BALs in strongly radio-loud objects suggests a similar mechanism may apply to quasars, it is clear that jets and winds can coexist in at least some RLQs. Further X-ray studies can help clarify the relationship between jets and outflows in RLQs: snapshot *Chandra* observations of additional BAL RLQs could permit more quantitative consideration of various physical models, while deep *XMM-Newton* spectral observations of the brightest BAL RLQs would help elucidate the properties of the X-ray absorber and perhaps differentiate them from those in BAL RQQs.

We gratefully acknowledge the financial support of NASA grant SAO SV4-74018 (G. P. G., Principal Investigator) and NASA LTSA grant NAG5-13035 (B. P. M., W. N. B.). We thank the referee for useful comments, Mike Eracleous for helpful discussions as well as assistance with HET/LRS data reduction and analysis, Jianfeng Wu for technical advice, and Chris Willot and Bob Becker/Rick White for providing us with electronic spectra of 4C +35.23 and FBQS 0256–0119, respectively.

Funding for the SDSS and SDSS-II has been provided by the Alfred P. Sloan Foundation, the Participating Institutions, the National Science Foundation, the U.S. Department of Energy, the National Aeronautics and Space Administration, the Japanese Monbukagakusho, the Max Planck Society, and the Higher Education Funding Council for England. The SDSS Web Site is <http://www.sdss.org/>.

The Hobby-Eberly Telescope (HET) is a joint project of the University of Texas at Austin, the Pennsylvania State University, Stanford University, Ludwig-Maximilians-Universität München, and Georg-August-Universität Göttingen. The HET is named in honor of its principal benefactors, William P. Hobby and Robert E. Eberly. The Marcario Low-Resolution Spectrograph is named for Mike Marcario of High Lonesome Optics, who fabricated several optics for the instrument but died before its completion; it is a joint project of the Hobby-Eberly Telescope partnership and the Instituto de Astronomía de la Universidad Nacional Autónoma de México.



## REFERENCES

- Anderson, S. F., Weymann, R. J., Foltz, C. B., & Chaffee, F. H., Jr. 1987, *AJ*, 94, 278
- Arav, N., Kaastra, J., Steenbrugge, K., Brinkman, B., Edelson, R., Korista, K. T., & de Kool, M. 2003, *ApJ*, 590, 174
- Avni, Y., & Tananbaum, H. 1986, *ApJ*, 305, 83
- Becker, R. H., White, R. L., & Helfand, D. J. 1995, *ApJ*, 450, 559
- Becker, R. H., Gregg, M. D., Hook, I. M., McMahon, R. G., White, R. L., & Helfand, D. J. 1997, *ApJ*, 479, L93
- Becker, R. H., White, R. L., Gregg, M. D., Brotherton, M. S., Laurent-Muehleisen, S. A., & Arav, N. 2000, *ApJ*, 538, 72
- Becker, R. H., et al. 2001, *ApJS*, 135, 227
- Benn, C. R., Carballo, R., Holt, J., Vigotti, M., González-Serrano, J. I., Mack, K.-H., & Perley, R. A. 2005, *MNRAS*, 360, 1455
- Brandt, W. N., Laor, A., & Wills, B. J. 2000, *ApJ*, 528, 637
- Brotherton, M. S., van Breugel, W., Smith, R. J., Boyle, B. J., Shanks, T., Croom, S. M., Miller, L., & Becker, R. H. 1998, *ApJ*, 505, L7
- Brotherton, M. S., Laurent-Muehleisen, S. A., Becker, R. H., Gregg, M. D., Telis, G., White, R. L., & Shang, Z. 2005, *AJ*, 130, 2006
- Brotherton, M. S., De Breuck, C., & Schaefer, J. J. 2006, *MNRAS*, 372, L58
- Condon, J. J., Cotton, W. D., Greisen, E. W., Yin, Q. F., Perley, R. A., Taylor, G. B., & Broderick, J. J. 1998, *AJ*, 115, 1693
- Douglas, J. N., Bash, F. N., Bozayan, F. A., Torrence, G. W., & Wolfe, C. 1996, *AJ*, 111, 1945
- Foltz, C. B., Chaffee, F. H., Jr., Hewett, P. C., MacAlpine, G. M., Turnshek, D. A., Weymann, R. J., & Anderson, S. F. 1987, *AJ*, 94, 1423
- Gallagher, S. C., Brandt, W. N., Chartas, G., & Garmire, G. P. 2002, *ApJ*, 567, 37
- Gallagher, S. C., Richards, G. T., Hall, P. B., Brandt, W. N., Schneider, D. P., & Vanden Berk, D. E. 2005, *AJ*, 129, 567
- Gallagher, S. C., Brandt, W. N., Chartas, G., Priddey, R., Garmire, G. P., & Sambruna, R. M. 2006, *ApJ*, 644, 709

- Gallagher, S. C., Hines, D. C., Blaylock, M., Priddey, R. S., Brandt, W. N., & Egami, E. E. 2007, *ApJ*, 665, 157
- Garmire, G. P., Bautz, M. W., Ford, P. G., Nousek, J. A., & Ricker, G. R., Jr. 2003, *Proc. SPIE*, 4851, 28
- Gehrels, N. 1986, *ApJ*, 303, 336
- Gibson, R. R., Brandt, W. N., & Schneider, D. P. 2008, *ApJ*, 685, 773
- Gibson, R. R., Brandt, W. N., Schneider, D. P., & Gallagher, S. C. 2008, *ApJ*, 675, 985
- Gibson, R. R., et al. 2009, *ApJ*, 692, 758
- Gopal-Krishna, & Wiita, P. J. 2000, *A&A*, 363, 507
- Green, P. J., Aldcroft, T. L., Mathur, S., Wilkes, B. J., & Elvis, M. 2001, *ApJ*, 558, 109
- Gregg, M. D., Becker, R. H., Brotherton, M. S., Laurent-Muehleisen, S. A., Lacy, M., & White, R. L. 2000, *ApJ*, 544, 142
- Gregg, M. D., Becker, R. H., & de Vries, W. 2006, *ApJ*, 641, 210
- Gregory, P. C., Scott, W. K., Douglas, K., & Condon, J. J. 1996, *ApJS*, 103, 427
- Hall, P. B., et al. 2002, *ApJS*, 141, 267
- Hall, P. B., Gallagher, S. C., Richards, G. T., Alexander, D. M., Anderson, S. F., Bauer, F., Brandt, W. N., & Schneider, D. P. 2006, *AJ*, 132, 1977
- Hewett, P. C., & Foltz, C. B. 2003, *AJ*, 125, 1784
- Hill, G. J., Nicklas, H. E., MacQueen, P. J., Tejada, C., Cobos Duenas, F. J., & Mitsch, W. 1998, *Proc. SPIE*, 3355, 375
- Ivezić, Ž., et al. 2002, *AJ*, 124, 2364
- Jester, S., Harris, D. E., Marshall, H. L., & Meisenheimer, K. 2006, *ApJ*, 648, 900
- Jiang, D. R., & Wang, T. G. 2003, *A&A*, 397, L13
- Jin, Y. K., Zhang, S. N., & Wu, J. F. 2006, *ApJ*, 653, 1566
- Just, D. W., Brandt, W. N., Shemmer, O., Steffen, A. T., Schneider, D. P., Chartas, G., & Garmire, G. P. 2007, *ApJ*, 665, 1004
- Kelly, B. C. 2007, *ApJ*, 665, 1489

- Kelly, B. C., Bechtold, J., Siemiginowska, A., Aldcroft, T., & Sobolewska, M. 2007, *ApJ*, 657, 116
- Kraft, R. P., Burrows, D. N., & Nousek, J. A. 1991, *ApJ*, 374, 344
- Kunert-Bajraszewska, M., & Marecki, A. 2007, *A&A*, 469, 437
- Lacy, M., Gregg, M., Becker, R. H., White, R. L., Glikman, E., Helfand, D., & Winn, J. N. 2002, *AJ*, 123, 2925
- Laor, A., & Brandt, W. N. 2002, *ApJ*, 569, 641
- Lavalley, M., Isobe, T., & Feigelson, E. 1992, *Astronomical Data Analysis Software and Systems I*, 25, 245
- Liu, Y., Jiang, D. R., Wang, T. G., & Xie, F. G. 2008, *MNRAS*, 391, 246
- Ma, F. 2002, *MNRAS*, 335, L99
- Menou, K., et al. 2001, *ApJ*, 561, 645
- Miller, B. P., Brandt, W. N., Gallagher, S. C., Laor, A., Wills, B. J., Garmire, G. P., & Schneider, D. P. 2006, *ApJ*, 652, 163
- Montenegro-Montes, F. M., Mack, K.-H., Vigotti, M., Benn, C. R., Carballo, R., González-Serrano, J. I., Holt, J., & Jiménez-Luján, F. 2008, *MNRAS*, 388, 1853
- Montenegro-Montes, F. M., Mack, K. -, Benn, C. R., Carballo, R., Dallacasa, D., González-Serrano, J. I., Holt, J., & Jiménez-Luján, F. 2009, *arXiv:0903.5119*
- Murray, N., Chiang, J., Grossman, S. A., & Voit, G. M. 1995, *ApJ*, 451, 498
- Neilsen, J., & Lee, J. C. 2009, *Nature*, 458, 481
- O’Dea, C. P. 1998, *PASP*, 110, 493
- Ogle, P. M., Cohen, M. H., Miller, J. S., Tran, H. D., Goodrich, R. W., & Martel, A. R. 1999, *ApJS*, 125, 1
- Page, K. L., Reeves, J. N., O’Brien, P. T., & Turner, M. J. L. 2005, *MNRAS*, 364, 195
- Perley, R. A., Condon, J. J., Cotton, W. D., Cohen, A. S., Lane, W. M., Kassim, N. E., Lazio, T. J. W., & Erickson, W. C. 2006, *VizieR Online Data Catalog*, 8079, 0
- Proga, D., Stone, J. M., & Kallman, T. R. 2000, *ApJ*, 543, 686
- Ramsey, L. W., et al. 1998, *Proc. SPIE*, 3352, 34

- Reeves, J. N., & Turner, M. J. L. 2000, *MNRAS*, 316, 234
- Reichard, T. A., et al. 2003, *AJ*, 126, 2594
- Rengelink, R. B., Tang, Y., de Bruyn, A. G., Miley, G. K., Bremer, M. N., Roettgering, H. J. A., & Bremer, M. A. R. 1997, *A&AS*, 124, 259
- Sambruna, R. M., Gliozzi, M., Tavecchio, F., Maraschi, L., & Foschini, L. 2006, *ApJ*, 652, 146
- Schaefer, J. J., Brotherton, M. S., Shang, Z., Gregg, M. D., Becker, R. H., Laurent-Muehleisen, S. A., Lacy, M., & White, R. L. 2006, *AJ*, 132, 1464
- Schneider, D. P., et al. 2007, *AJ*, 134, 102
- Shankar, F., Dai, X., & Sivakoff, G. R. 2008, *ApJ*, 687, 859
- Siemiginowska, A., LaMassa, S., Aldcroft, T. L., Bechtold, J., & Elvis, M. 2008, *ApJ*, 684, 811
- Stawarz, L., Ostorero, L., Begelman, M. C., Moderski, R., Kataoka, J., & Wagner, S. 2008, *ApJ*, 680, 911
- Steffen, A. T., Strateva, I., Brandt, W. N., Alexander, D. M., Koekemoer, A. M., Lehmer, B. D., Schneider, D. P., & Vignali, C. 2006, *AJ*, 131, 2826
- Stocke, J. T., Morris, S. L., Weymann, R. J., & Foltz, C. B. 1992, *ApJ*, 396, 487
- Strateva, I. V., Brandt, W. N., Schneider, D. P., Vanden Berk, D. G., & Vignali, C. 2005, *AJ*, 130, 387
- Trump, J. R., et al. 2006, *ApJS*, 165, 1
- Urrutia, T., Lacy, M., Gregg, M. D., & Becker, R. H. 2005, *ApJ*, 627, 75
- Urrutia, T., Lacy, M., & Becker, R. H. 2008, *ApJ*, 674, 80
- Urrutia, T., Becker, R. H., White, R. L., Glikman, E., Lacy, M., Hodge, J., & Gregg, M. D. 2009, *ApJ*, 698, 1095
- Vanden Berk, D. E., et al. 2001, *AJ*, 122, 549
- de Vries, W. H., Becker, R. H., & White, R. L. 2006, *AJ*, 131, 666
- Wang, J., Jiang, P., Zhou, H., Wang, T., Dong, X., & Wang, H. 2008, *ApJ*, 676, L97
- Weymann, R. J., Morris, S. L., Foltz, C. B., & Hewett, P. C. 1991, *ApJ*, 373, 23
- White, R. L., Becker, R. H., Helfand, D. J., & Gregg, M. D. 1997, *ApJ*, 475, 479

- White, R. L., et al. 2000, *ApJS*, 126, 133
- Wilkes, B. J., & Elvis, M. 1987, *ApJ*, 323, 243
- Willott, C. J., Rawlings, S., Archibald, E. N., & Dunlop, J. S. 2002, *MNRAS*, 331, 435
- Willott, C. J., Rawlings, S., & Grimes, J. A. 2003, *ApJ*, 598, 909
- Wills, B. J., & Brotherton, M. S. 1995, *ApJ*, 448, L81
- Wills, B. J., Brandt, W. N., & Laor, A. 1999, *ApJ*, 520, L91
- Worrall, D. M., Tananbaum, H., Giommi, P., & Zamorani, G. 1987, *ApJ*, 313, 596
- Wu, J. F., Zhang, S. N., Lu, F. J., & Jin, Y. K. 2007, *Chinese Journal of Astronomy and Astrophysics*, 7, 81
- York, D. G., et al. 2000, *AJ*, 120, 1579
- Zhou, H., Wang, T., Wang, H., Wang, J., Yuan, W., & Lu, Y. 2006, *ApJ*, 639, 716

Table 1. *Chandra* and *HET* Observing Log

Name (SDSS)	ObsID	<i>Chandra</i> Observations			<i>HET</i> Observations			
		Date	Exp (s)	Counts <sup>a</sup>	Date	Exp (s)	$\lambda/\Delta\lambda^b$	S/N <sup>c</sup>
074610.50+230710.8 ...	9160	2007 Dec 12	6954	$67.9^{+9.3}_{-8.2}$	2007 Dec 18	1200	867	10
083749.59+364145.4 ...	9153	2007 Dec 23	6101	$17.7^{+5.3}_{-4.2}$	2007 Dec 18	1800	867	20
085641.58+424254.1 ...	9156	2008 Feb 10	5968	$17.0^{+5.2}_{-4.1}$	2008 Feb 24	1500	867	18
092913.96+375742.9 ...	9162	2007 Dec 28	3987	$47.6^{+7.9}_{-6.9}$	...	...	...	...
102258.41+123429.7 ...	9154	2008 Apr 04	4976	$24.1^{+6.0}_{-4.9}$	2008 May 03	900	300	26
105416.51+512326.0 ...	9163	2008 Jan 20	4979	$36.7^{+7.1}_{-6.0}$	2008 Feb 08	1500	867	19
112506.95-001647.6 ...	9157	2008 Apr 29	5112	$80.1^{+10.0}_{-8.9}$	...	...	...	...
115944.82+011206.9 ...	9158	2007 Feb 28	3706	$171.1^{+14.1}_{-13.1}$	2008 Feb 13	900	867	37
123411.73+615832.6 ...	9152	2008 Feb 22	6142	$17.4^{+5.2}_{-4.1}$	2008 Apr 23	1500	867	29
133701.39-024630.3 ...	9159	2007 Dec 10	4692	$23.3^{+5.9}_{-4.8}$	2008 Feb 08	1500	867	17
141334.38+421201.7 ...	9161	2008 Apr 03	6954	$48.6^{+8.0}_{-6.9}$	2008 May 08	1200	650	36
162453.47+375806.6 ...	9155	2007 Nov 25	3994	$18.3^{+5.4}_{-4.2}$	2008 Feb 08	1300	867	15

Note. — All targets were observed with *Chandra* on-axis with the ACIS-S array, using Very Faint mode. *HET* spectra were obtained with the Low Resolution Spectrograph; 10/12 targets were able to be observed.

<sup>a</sup>Background-subtracted and aperture-corrected counts in the 0.5–8 keV band. Errors are  $1\sigma$  (Poisson errors; Gehrels 1986). All snapshot targets are detected.

<sup>b</sup>Most observations were conducted using the g2 grism with a  $1.5''$  slit, providing a resolving power of 867.

<sup>c</sup>Signal-to-noise of the continuum near observed-frame 6000 Å.

Table 2. *Chandra* Archival Sources

Name (SDSS)	Name (Other)	ObsID	Date	Exp (s)	$\theta$ (')	Counts <sup>b</sup>	Sel <sup>c</sup>	Ref
020022.01–084512.0	FBQS J0200–0845 . . . . .	3265	2002 Oct 02	17901	9.4	$55.3^{+8.5}_{-7.4}$	S	1
...	FBQS J0256–0119 . . . . .	850	1999 Dec 09	4456	0.0	$18.8^{+5.4}_{-4.3}$	L	2
081426.45+364713.5	. . . . .	3436	2002 Jan 31	9839	8.3	$8.8^{+4.1}_{-2.9}$	S	...
081426.45+364713.5 <sup>d</sup>	. . . . .	3437	2002 Feb 11	9933	8.3	$9.5^{+4.2}_{-3.0}$	S	...
091951.29+005854.9	. . . . .	7056	2006 Jun 28	5080	4.3	< 3.6	S	...
100726.10+124856.2	PG 1004+130 . . . . .	5606	2005 Jan 05	41064	0.0	$1851.4^{+44.0}_{-43.0}$	L	3
104834.24+345724.9	4C +35.23 . . . . .	9320	2008 Jan 20	4658	0.0	$5.5^{+3.5}_{-2.3}$	L	4
122033.87+334312.0	3C 270.1 . . . . .	2118	2002 Apr 03	3087	4.3	$177.4^{+14.3}_{-13.3}$	S	...
131213.57+231958.6	FBQS J131213.5+231958	852	2000 May 19	4686	0.0	$58.8^{+8.7}_{-7.6}$	L	2
...	LBQS 2211–1915 . . . . .	4836	2003 Nov 19	5889	0.0	$53.8^{+8.4}_{-7.3}$	L	5

<sup>a</sup>Off-axis angle in arc-minutes; a value of 0.0 indicates an observation targeting that BAL RLQ.

<sup>b</sup>Background-subtracted and aperture-corrected counts in the 0.5–8 keV band. Errors are  $1\sigma$  (Poisson errors; Gehrels 1986), while limits for non-detections are at the 95% confidence level (Bayesian statistics; Kraft et al. 1991).

<sup>c</sup>Selection method: S = BAL RLQ identified from SDSS/FIRST data with serendipitous *Chandra* archival coverage, while L = BAL RLQ identified from literature with targeted *Chandra* archival coverage.

<sup>d</sup>Since the two observations of 081426.45+364713.5 are of comparable quality, both are shown; these observations are stacked for later analysis. There are  $18.3^{+5.4}_{-4.2}$  net 0.5–8 keV counts in the combined 19.8 ks exposure.

References. — Prior analysis of *Chandra* data: (1) Gallagher et al. (2005); (2) Brotherton et al. (2005); Miller et al. (2006); (4) PI Kunert-Bajraszewska; (5) Gallagher et al. (2006).

Table 3. Optical/UV Characteristics

Name (SDSS)	$z$	$m_i$	$M_i$	$\Delta(g-i)$	BI	AI	EW	$V_{\max}$	Type <sup>a</sup>	Ref
Snapshot BAL RLQs										
074610.50+230710.8.....	2.093	18.27	−27.19	1.057	...	2955	14.4 <sup>b</sup>	5225	Hi	1
083749.59+364145.4.....	3.416	18.55	−28.01	0.614	4243.0	6881	34.6	11472	HL	2
085641.58+424254.1.....	3.062	18.41	−27.91	0.106	820.6	2660	12.8	8071	H	2
092913.96+375742.9.....	1.915	17.51	−27.76	0.562	0.0	2630	13.4	4166	Hi	2
102258.41+123429.7.....	1.729	17.86	−27.16	0.562	1008.7	...	10.1	10180	Hi	2
105416.51+512326.0.....	2.341	18.48	−27.24	0.352	337.5	2177	9.7	5669	H	2
112506.95−001647.6.....	1.770	18.86	−26.22	0.264	0.0	1743	7.1	3897	Hi	2
115944.82+011206.9.....	2.000	16.96	−28.40	0.412	0.0	2887	12.5	4331	Hi	2
123411.73+615832.6.....	1.946	18.39	−26.90	0.442	4907.9	10718	32.4	20020	Hi	2
133701.39−024630.3.....	3.064	18.41	−27.91	0.242	0.0	1657	5.3	4983	H	2
141334.38+421201.7.....	2.817	18.24	−27.89	0.516	0.0	2688	15.0	4861	H	2
162453.47+375806.6.....	3.381	18.15	−28.38	0.281	2990.0	4156	13.6 <sup>b</sup>	28300	H	3
Archival BAL RLQs										
020022.01−084512.0.....	1.943	18.28	−27.01	0.484	2788.2	4135	19.9	14231	Hi	2
FBQS J0256−0119.....	2.490	18.40	−27.46	0	250.0	...	12.9 <sup>b</sup>	12400 <sup>b</sup>	H	4
081426.45+364713.5.....	2.732	19.81	−26.26	1.104	2438.40	5289	26.2	8300	HLF	2
091951.29+005854.9.....	2.114	19.45	−26.04	0.130	673.1	1268	6.9	22041	nHi	2
100726.10+124856.2.....	0.241	15.20	−25.09	−0.45	850.0	...	14.7 <sup>b</sup>	10000	Hi	5
104834.24+345724.9.....	1.594	20.17	−24.66	0.88	...	...	26.2 <sup>b</sup>	14300 <sup>b</sup>	Hi	6
122033.87+334312.0.....	1.532	18.10	−26.64	0.398	52.5	...	6.5	5266	HL	2
131213.57+231958.6.....	1.508	17.11	−27.59	0.084	1400.0	...	15.6 <sup>b</sup>	25000	Hi	7
LBQS 2211−1915.....	1.952	17.34	−27.96	0.32	27.0	...	7.8	11544	Hi	8,9

Note. — The  $k$ -correction for  $M_i$  assumes a power-law continuum with spectral index  $\alpha_\nu = -0.5$ . The absorption properties refer to C IV measurements. BI, EW, and  $V_{\max}$  values are primarily from the listed reference, chiefly Gibson et al. (2009), while AI values are taken from Trump et al. (2006) where available. The units for BI, AI, and  $V_{\max}$  are  $\text{km s}^{-1}$ ; EW is in Å.

<sup>a</sup>BAL type following Trump et al. (2006): Hi = HiBAL (no Mg II absorption in spectrum); HLF = FeLoBAL (C IV BAL, Fe II or Fe III absorption in spectrum); HL = HiBAL with some low-ionization absorption; H = HiBAL lacking spectral coverage of Mg II; n = relatively narrow absorption. Type is taken from Trump et al. (2006) for all quasars with reported AI measurements; the remainder are classified based on our examination of the SDSS spectrum where available or else by the listed reference.

<sup>b</sup>EW or  $V_{\max}$  value measured by us.

References. — (1) Trump et al. (2006); (2) Gibson et al. (2009); Benn et al. (2005); (4) Becker et al. (2001); (5) Wills et al. (1999); (6) Willott et al. (2002); (7) Becker et al. (2000); (8) Weymann et al. (1991); (9) Gallagher et al. (2006).



Table 4. Radio Characteristics

Name (SDSS)	Type <sup>c</sup>	Flux-Density Measurements <sup>a</sup>				Spectral Indices <sup>b</sup>	
		≤365 MHz	1.4 GHz (F)	1.4 GHz (N)	4.85 GHz	α <sub>low</sub>	α <sub>high</sub>
Snapshot BAL RLQs							
074610.50+230710.8 . . . . .	P	...	23.68	22.3±0.8	27±4 G	...	+0.11
083749.59+364145.4 . . . . .	P	...	27.10	...	...	...	-0.43
085641.58+424254.1 . . . . .	P	...	19.99	20.2±0.7	29±4 G	...	+0.30
092913.96+375742.9 . . . . .	P	94 W	43.43	42.9±1.3	24±4 G	-0.53	-0.48
102258.41+123429.7 . . . . .	D	448±51 T	118.65 <sup>d</sup>	126.1±3.8	44±6 G	-0.99	-0.80
105416.51+512326.0 . . . . .	P	44 W	33.88	35.6±1.1	22±4 G	-0.18	-0.35
112506.95-001647.6 . . . . .	D	890±130 V	65.47 <sup>d</sup>	74.0±2.7	...	-0.89	...
115944.82+011206.9 . . . . .	P	887±30 T	268.48	275.6±8.3	137.8±1.7 M	-0.89	-0.54
123411.73+615832.6 . . . . .	P	...	23.96	22.7±0.8	13.2 C	...	-0.48
133701.39-024630.3 . . . . .	P	...	44.82	45.1±1.4	39.4 C	...	-0.10
141334.38+421201.7 . . . . .	P	22 W	18.74	16.8±0.6	8.8±0.7 M	-0.11	-0.61
162453.47+375806.6 . . . . .	P	72 W	56.44	55.6±1.7	23.3±1.1 B	-0.17	-0.71
Archival BAL RLQs							
020022.01-084512.0 . . . . .	P	...	7.34	8.0±0.5	...	...	...
FBQS J0256-0119 . . . . .	P	...	27.56	22.3±0.8	12.0±0.5 M	...	-0.67
081426.45+364713.5 . . . . .	P	...	2.98	3.8±0.4	...	...	...
091951.29+005854.9 . . . . .	P	...	2.78	2.6±0.5	...	...	...
100726.10+124856.2 . . . . .	D	2740 P	... <sup>d</sup>	1216.1±29.6 <sup>d</sup>	415±37 G	-0.66	-0.87
104834.24+345724.9 . . . . .	P	2437±29 T	1050.97	1034.4±31.0	439±39 G	-0.63	-0.70
122033.87+334312.0 . . . . .	D	9742±134 T	2819.00 <sup>d</sup>	2845.9±85.4	842±75 G	-0.92	-0.97
131213.57+231958.6 . . . . .	P	...	44.12	46.5±1.4	25.7±0.6 M	...	-0.43
LBQS 2211-1915 . . . . .	P	...	...	64.0±2.0	...	...	...

<sup>a</sup>All flux density measurements are in mJy, taken from the following sources: B = Benn et al. (2005); C = archival VLA C-band imaging; F = FIRST: Faint Images of the Radio Sky at Twenty cm, integrated flux, RMS errors are  $\simeq 0.15$  mJy beam<sup>-1</sup> (White et al. 1997); G = Green Bank 6-cm survey (Gregory et al. 1996); M = Montenegro-Montes et al. (2008); N = NVSS: NRAO VLA Sky Survey (Condon et al. 1998); P = Parkes Catalogue 1990, 408 MHz; T = Texas Survey of Radio Sources at 365 MHz (Douglas et al. 1996); V = VLA Low-Frequency Sky Survey, 74 MHz (Perley et al. 2006); W = Westerbork Northern Sky Survey, 326 MHz, RMS errors are  $\simeq 4$  mJy beam<sup>-1</sup> (Rengelink et al. 1997).

<sup>b</sup>Radio spectral indices include extended emission components, are given as  $S_{\nu} \propto \nu^{\alpha_{\nu}}$ , and use FIRST measurements where available (else NVSS measurements); the quantities  $\alpha_{\text{low}}$  and  $\alpha_{\text{high}}$  are calculated from the flux densities presented in the columns labeled  $\leq 365$  MHz and 4.85 GHz, respectively, in addition to the 1.4 GHz data. J083749.59+364145.4 has a bright unrelated radio source  $\sim 50''$  North of the core that contaminates low-resolution maps; the spectral index is from a high-resolution 8.45 GHz flux density measurement from Montenegro-Montes et al. (2008).

<sup>c</sup>Radio morphology: P = point source, D = double (lobes summed for flux measurements). See §3.3 for comments.

<sup>d</sup>Extended emission: J102258.41+123429.7 has two FIRST components offset from the SDSS position by 0.058' and 0.174', with integrated fluxes of 93.98 and 24.67 mJy, respectively; J112506.95-001647.6 has two FIRST components offset from the SDSS position by 0.099' and 0.201', with integrated fluxes of 55.36 and 10.11 mJy, respectively; J100726.10+124856.2 (PG 1004+130) is over-resolved by FIRST, but has two NVSS components offset from the SDSS position by 0.434' and 1.010', with fluxes of 656.4 and 559.7 mJy, respectively; J122033.87+334312.0 (3C 270.1) has two FIRST components offset from the SDSS position by 0.067' and 0.073', with integrated fluxes of 2096.61 and 722.39 mJy, respectively.

Table 5. X-ray Counts, Luminosities, and Properties of BAL RLQs

Name (SDSS)	Soft	X-ray Counts <sup>a</sup>			Rate	Luminosities <sup>b</sup>			Derived Properties <sup>c</sup>				
		Hard	$HR$			$l_r$	$l_{uv}$	$l_x$	$R^*$	$\alpha_{ox}$	$\Delta l_{x,uv}$	$\Delta l_{x,S}$	$\Delta l_{x,H}$
Snapshot BAL RLQs													
074610.50+230710.8	49.4 <sup>+8.1</sup> <sub>-7.0</sub>	17.6 <sup>+5.3</sup> <sub>-4.2</sub>	-0.47 <sup>+0.11</sup> <sub>-0.10</sub>	9.8 <sup>+1.3</sup> <sub>-1.2</sub>	33.36	31.15	27.01	2.21	-1.59	-0.37	-0.06	-0.15	
083749.59+364145.4	13.6 <sup>+4.8</sup> <sub>-3.6</sub>	< 3.5	< -0.59	2.9 <sup>+0.9</sup> <sub>-0.7</sub>	33.85	31.53	26.91	2.32	-1.77	-0.81	-0.52	< -0.7	
085641.58+424254.1	11.5 <sup>+4.5</sup> <sub>-3.3</sub>	6.1 <sup>+3.6</sup> <sub>-2.4</sub>	-0.31 <sup>+0.24</sup> <sub>-0.19</sub>	2.8 <sup>+0.9</sup> <sub>-0.7</sub>	33.63	31.43	26.79	2.20	-1.78	-0.84	-0.55	-0.45	
092913.96+375742.9	26.3 <sup>+6.2</sup> <sub>-5.1</sub>	21.0 <sup>+5.6</sup> <sub>-4.5</sub>	-0.11 <sup>+0.14</sup> <sub>-0.14</sub>	11.9 <sup>+2.0</sup> <sub>-1.7</sub>	33.54	31.40	26.99	2.15	-1.69	-0.61	-0.40	-0.11	
102258.41+123429.7	15.8 <sup>+5.1</sup> <sub>-3.9</sub>	7.7 <sup>+3.9</sup> <sub>-2.7</sub>	-0.34 <sup>+0.20</sup> <sub>-0.17</sub>	4.9 <sup>+1.2</sup> <sub>-1.0</sub>	33.83	31.13	26.52	2.71	-1.77	-0.84	-0.78	-0.72	
105416.51+512326.0	26.0 <sup>+6.2</sup> <sub>-5.1</sub>	11.0 <sup>+4.4</sup> <sub>-3.3</sub>	-0.41 <sup>+0.16</sup> <sub>-0.13</sub>	7.4 <sup>+1.4</sup> <sub>-1.2</sub>	33.62	31.27	26.96	2.35	-1.65	-0.53	-0.29	-0.27	
112506.95-001647.6	59.5 <sup>+8.8</sup> <sub>-7.7</sub>	24.3 <sup>+6.0</sup> <sub>-4.9</sub>	-0.42 <sup>+0.13</sup> <sub>-0.09</sub>	15.7 <sup>+2.0</sup> <sub>-1.7</sub>	33.60	30.74	27.05	2.86	-1.42	+0.04	+0.08	+0.05	
115944.82+011206.9	93.1 <sup>+10.7</sup> <sub>-9.6</sub>	80.1 <sup>+10.0</sup> <sub>-8.9</sub>	-0.08 <sup>+0.08</sup> <sub>-0.08</sub>	46.2 <sup>+3.8</sup> <sub>-3.5</sub>	34.38	31.67	27.62	2.70	-1.56	-0.23	-0.24	+0.07	
123411.73+615832.6	11.6 <sup>+4.5</sup> <sub>-3.3</sub>	5.4 <sup>+3.5</sup> <sub>-2.3</sub>	-0.36 <sup>+0.24</sup> <sub>-0.19</sub>	2.8 <sup>+0.9</sup> <sub>-0.7</sub>	33.30	31.06	26.38	2.24	-1.80	-0.92	-0.67	-0.61	
133701.39-024630.3	10.5 <sup>+4.3</sup> <sub>-3.2</sub>	12.2 <sup>+4.6</sup> <sub>-3.4</sub>	0.07 <sup>+0.20</sup> <sub>-0.20</sub>	5.0 <sup>+1.3</sup> <sub>-1.0</sub>	33.98	31.48	27.04	2.50	-1.70	-0.63	-0.65	-0.21	
141334.38+421201.7	34.7 <sup>+6.9</sup> <sub>-5.9</sub>	16.5 <sup>+5.1</sup> <sub>-4.0</sub>	-0.35 <sup>+0.14</sup> <sub>-0.12</sub>	7.0 <sup>+1.2</sup> <sub>-1.0</sub>	33.53	31.56	27.10	1.97	-1.71	-0.65	-0.24	-0.18	
162453.47+375806.6	13.4 <sup>+4.7</sup> <sub>-3.6</sub>	5.5 <sup>+3.5</sup> <sub>-2.3</sub>	-0.42 <sup>+0.23</sup> <sub>-0.17</sub>	4.6 <sup>+1.3</sup> <sub>-1.1</sub>	34.17	31.74	27.08	2.43	-1.79	-0.83	-0.61	-0.60	
Archival BAL RLQs													
020022.01-084512.0	38.4 <sup>+7.2</sup> <sub>-6.2</sub>	14.9 <sup>+4.9</sup> <sub>-3.8</sub>	-0.58 <sup>+0.13</sup> <sub>-0.11</sub>	3.1 <sup>+0.5</sup> <sub>-0.4</sub>	32.79	31.11	26.52	1.68	-1.76	-0.82	-0.31	-0.36	
FBQS J0256-0119	15.4 <sup>+5.0</sup> <sub>-3.9</sub>	4.4 <sup>+3.2</sup> <sub>-2.0</sub>	-0.56 <sup>+0.21</sup> <sub>-0.15</sub>	4.2 <sup>+1.2</sup> <sub>-1.0</sub>	33.50	31.51	26.77	1.99	-1.82	-0.93	-0.51	-0.59	
081426.45+364713.5	10.2 <sup>+4.3</sup> <sub>-3.1</sub>	7.5 <sup>+3.8</sup> <sub>-2.7</sub>	-0.29 <sup>+0.23</sup> <sub>-0.21</sub>	0.9 <sup>+0.3</sup> <sub>-0.2</sub>	32.70	30.71	26.33	1.99	-1.68	-0.65	-0.38	-0.17	
091951.29+005854.9	< 3.3	< 3.5	...	< 0.7	32.44	30.74	<26.0	1.71	<-1.8	<-1.0	<-0.3	<-0.0	
100726.10+124856.2	1107 <sup>+34.3</sup> <sub>-33.3</sub>	794 <sup>+29.2</sup> <sub>-28.2</sub>	-0.16 <sup>+0.02</sup> <sub>-0.02</sub>	45.1 <sup>+1.1</sup> <sub>-1.0</sub>	32.86	30.52	25.66	2.34	-1.87	-1.15	-0.99	-0.77	
104834.24+345724.9	< 3.2	4.4 <sup>+3.2</sup> <sub>-2.0</sub>	> 0.16	1.2 <sup>+0.7</sup> <sub>-0.5</sub>	34.76	30.48	25.82	4.28	-1.79	-0.95	<-1.6	-1.10	
122033.87+334312.0	134.1 <sup>+12.6</sup> <sub>-11.6</sub>	47.6 <sup>+7.9</sup> <sub>-6.9</sub>	-0.48 <sup>+0.10</sup> <sub>-0.10</sub>	57.5 <sup>+4.6</sup> <sub>-4.3</sub>	35.07	30.89	27.41	4.19	-1.34	+0.27	-0.26	-0.20	
131213.57+231958.6	48.4 <sup>+8.0</sup> <sub>-6.9</sub>	11.0 <sup>+4.4</sup> <sub>-3.3</sub>	-0.63 <sup>+0.11</sup> <sub>-0.09</sub>	12.5 <sup>+1.9</sup> <sub>-1.6</sub>	33.30	31.42	26.74	1.88	-1.80	-0.88	-0.42	-0.55	
LBQS 2211-1915	38.4 <sup>+7.2</sup> <sub>-6.2</sub>	16.6 <sup>+5.1</sup> <sub>-4.0</sub>	-0.40 <sup>+0.13</sup> <sub>-0.11</sub>	9.1 <sup>+1.4</sup> <sub>-1.2</sub>	33.78	31.67	26.87	2.11	-1.84	-0.98	-0.66	-0.54	

<sup>a</sup>The soft and hard bands are 0.5–2 keV and 2–8 keV, respectively; errors/limits are as in Tables 1 and 2. The hardness ratio is  $HR = (H - S)/(H + S)$ , where  $S$  ( $H$ ) is the soft (hard) band counts; errors are  $1\sigma$ . The  $HR$  values for J020022.01-084512.0 and J081426.45+364713.5, observed with ACIS-I, have been adjusted by subtracting 0.14 to enable direct comparison to the ACIS-S  $HR$  values. Rate is counts  $\text{ks}^{-1}$  in the 0.5–8 keV band.

<sup>b</sup>These monochromatic luminosities have units of  $\log \text{ergs s}^{-1} \text{Hz}^{-1}$ , at rest-frame frequencies of 5 GHz, 2500 Å, and 2 keV for  $l_r$ ,  $l_{uv}$ , and  $l_x$ , respectively.  $l_x$  is calculated from the 0.5–8 keV count rates for a power-law of  $\Gamma = 1.5$  and is corrected for Galactic absorption.

<sup>c</sup>The radio loudness (in log units) is  $R^* = l_r - l_{uv}$  and the optical/UV-to-X-ray spectral slope is  $\alpha_{ox} = 0.3838 \times (l_x - l_{uv})$ . The relative X-ray luminosities are  $\Delta l_{x,uv} = l_x - (0.905 \times l_{uv} - 0.813)$  and  $\Delta l_{x,S/H} = l_{x,S/H} - (0.472 \times l_{uv} + 0.413 \times l_r - 1.392)$ , where  $l_{x,S}$  and  $l_{x,H}$  are 2 keV X-ray luminosities calculated from the 0.5–2 keV and 2–8 keV count rates, respectively.

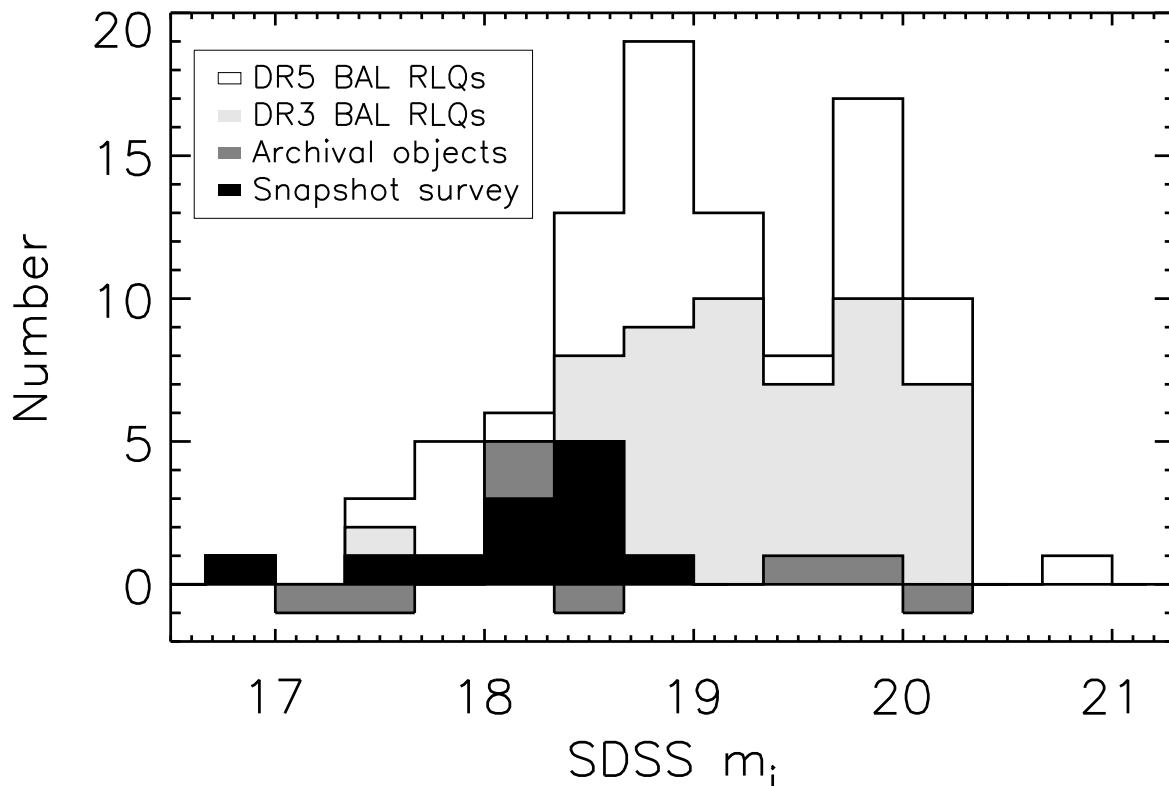


Fig. 1.— Histogram showing the SDSS  $m_i$  distribution for radio-loud broad absorption line quasars satisfying  $R^* \gtrsim 100$  and  $EW_{\text{CIV}} > 5\text{\AA}$ . The light gray shaded area indicates the subset of BAL RLQs that had spectra available in SDSS DR3 or earlier, and the filled area shows those objects selected for the snapshot survey (black, 12 objects) or possessing archival *Chandra* coverage (dark gray, 8 objects shown; PG 1004+130 has  $m_i = 15.2$ ). Archival objects selected from the literature are plotted on a negative scale.

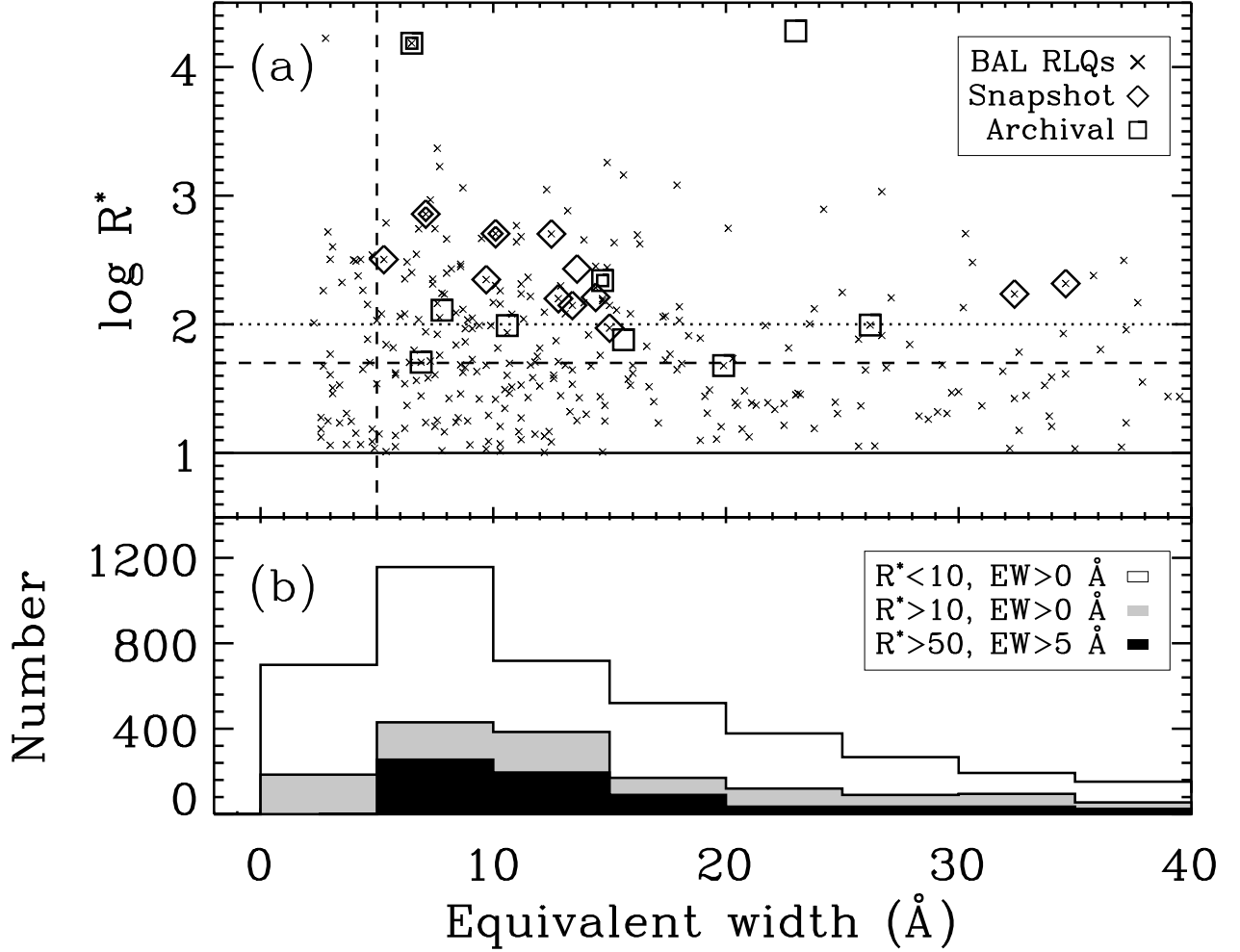


Fig. 2.— (a) Radio loudness plotted versus broad absorption line strength (parameterized by C IV EW). The *Chandra* snapshot BAL RLQs are shown as diamonds and the archival BAL RLQs as squares (nested symbols are lobe-dominated BAL RLQs). The solid line marks the  $R^* > 10$  ( $\log R^* > 1$ ) boundary, below which quasars are defined to be radio-quiet. The dashed lines show the selection criteria for the archival sample of BAL RLQs, which were required to be definitively radio-loud ( $R^* \gtrsim 50$ ) and show strong broad absorption lines ( $EW > 5 \text{ \AA}$ ). The dotted line shows the more restrictive criteria of  $R^* \gtrsim 100$  that was used to select the snapshot sample. As reported by previous authors it is rare for quasars to be simultaneously strongly absorbed and strongly radio-loud. (b) Plot of the distribution of C IV EW for objects with  $R^* < 10$  (open histogram), objects with  $R^* > 10$  (gray histogram), and objects with  $R^* > 50$  and  $EW > 5 \text{ \AA}$  (black histogram). Numbers for objects with  $R^* > 10$  (the gray and black histograms) have been multiplied by 5 for clarity.

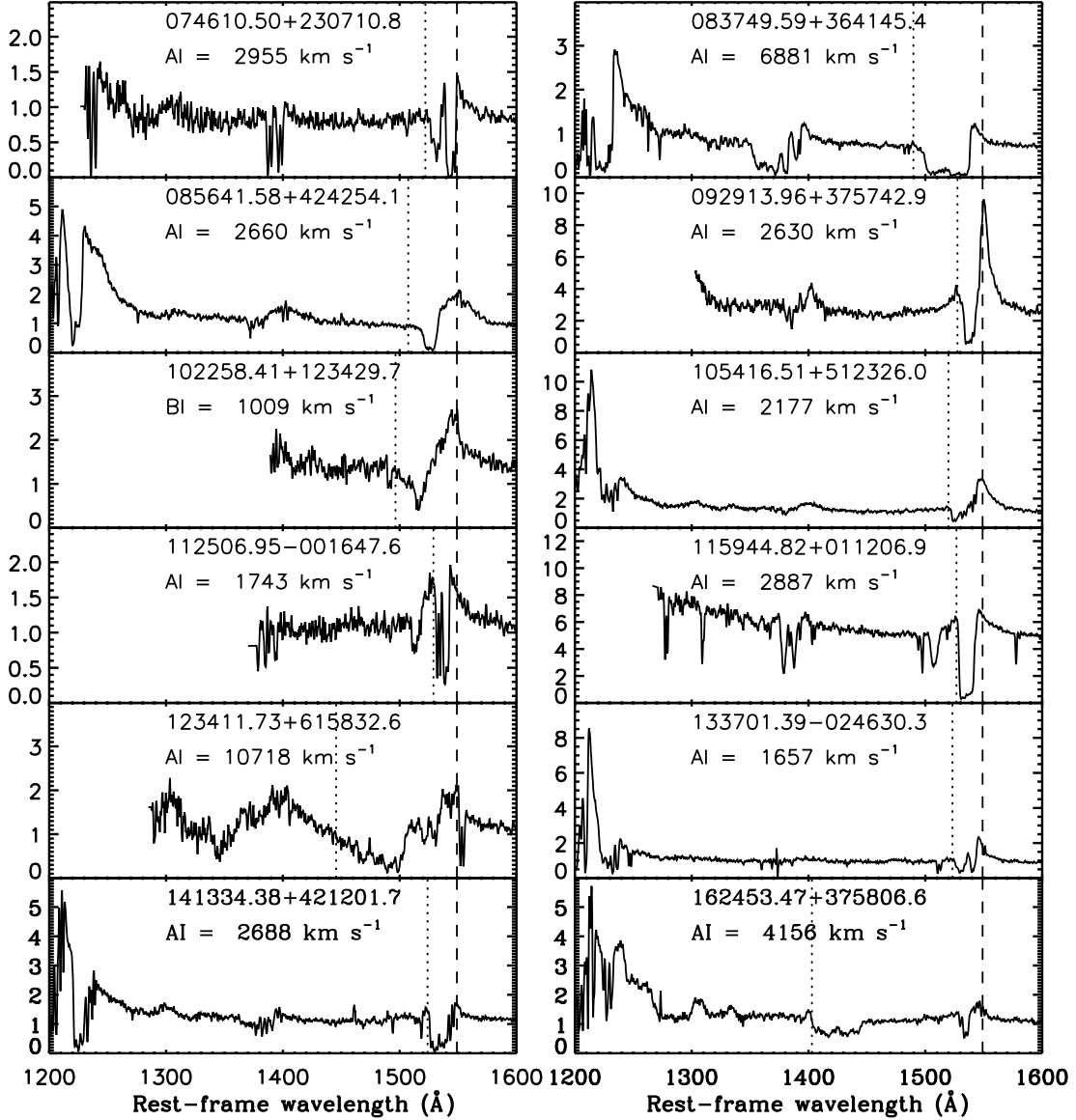


Fig. 3.— SDSS spectra for the snapshot sample, plotted with rest-frame wavelengths and showing the  $L\alpha$  to C IV BAL region. The dashed line in each panel is at 1549 Å, or zero velocity. The dotted line indicates the maximum outflow velocity, primarily taken from Gibson et al. (2009). Flux is given in units of  $10^{-16} \text{ erg cm}^{-2} \text{ s}^{-1} \text{ Å}^{-1}$ . The sample includes objects covering a range of BAL absorption strengths and outflow velocities. Each panel is labeled with the SDSS DR5 name as well as the absorption index (a measure of BAL strength), primarily taken from Trump et al. (2006).

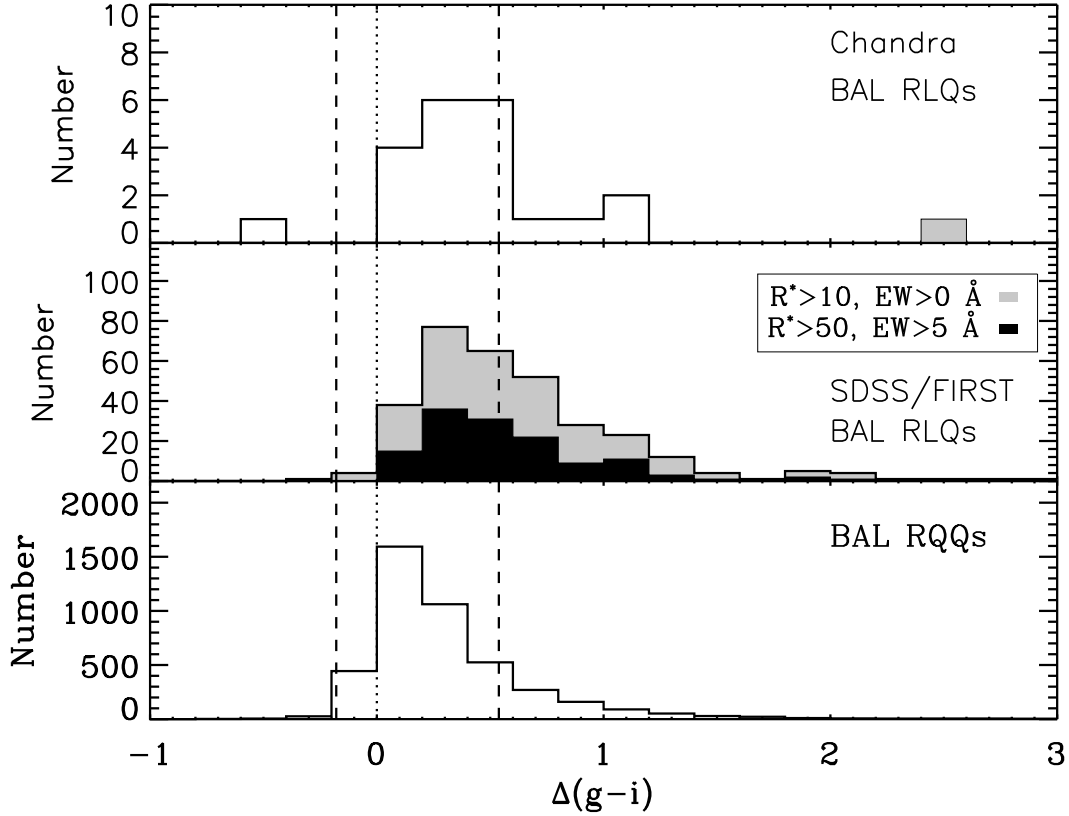


Fig. 4.— Relative color  $\Delta(g-i)$ , calculated by taking the measured  $(g-i)$  for a given object and subtracting the  $(g-i)$  that is typical for quasars at that redshift (positive values correspond to redder objects). The top panel shows the snapshot and archival sample of BAL RLQs with *Chandra* coverage (the object shaded in gray is the strongly reddened object FBQS J1556+3517, marked for comparison but not included in the archival sample). The middle panel shows SDSS/FIRST BAL RLQs, and the bottom panel shows BAL RQQs. The dashed lines enclose 90% of SDSS DR5 quasars. While BAL quasars tend to be redder than non-BAL quasars, the BAL RLQs studied with *Chandra* are representative of BAL RLQs in general and do not show excessive intrinsic reddening that could significantly elevate radio-loudness values.

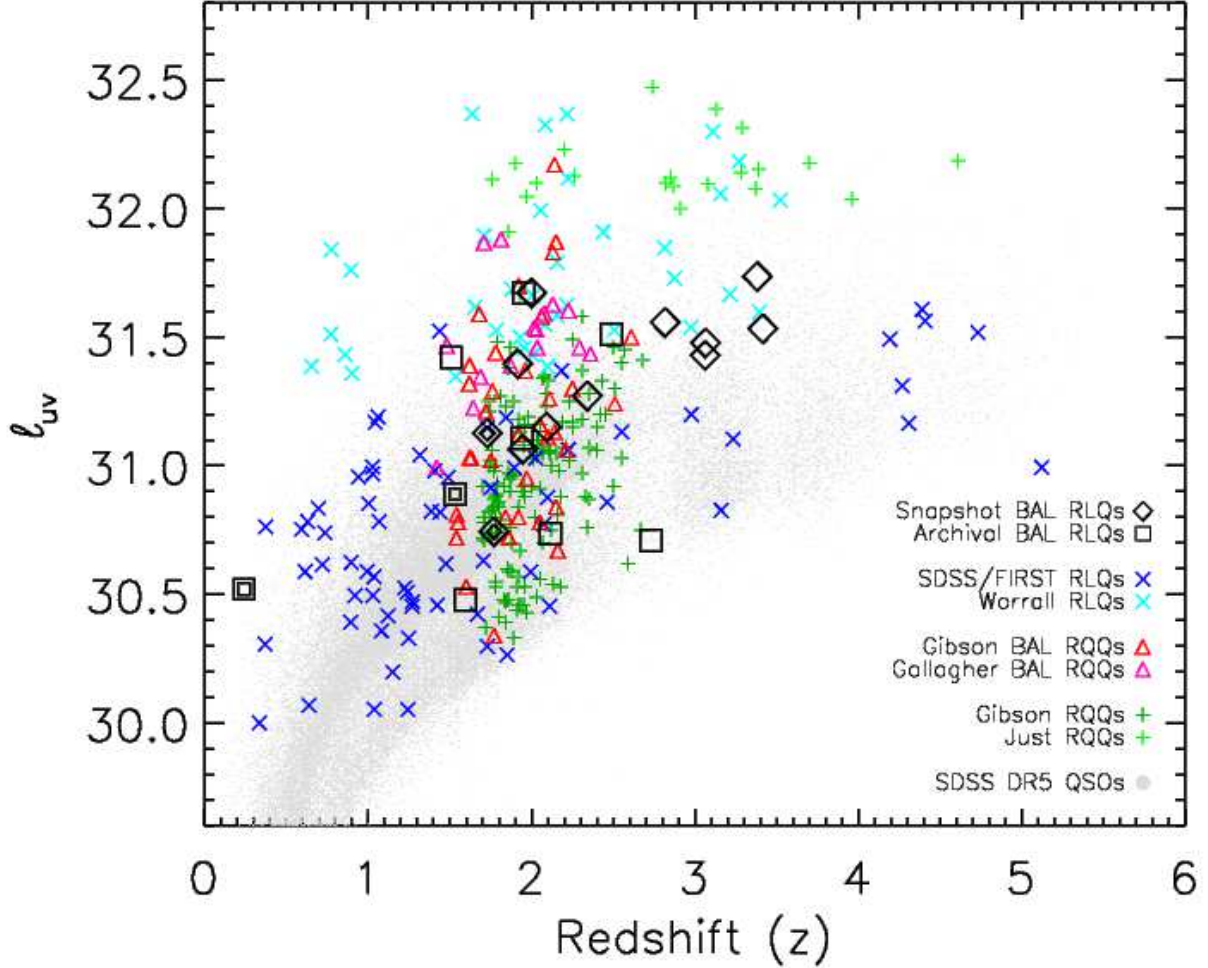


Fig. 5.— Optical luminosity  $l_{uv}$  in units of  $\log \text{ergs s}^{-1} \text{Hz}^{-1}$  calculated at rest-frame  $2500 \text{ \AA}$  for our sample of BAL RLQs (nested symbols are lobe-dominated BAL RLQs) and for comparison samples of non-BAL RLQs, BAL RQQs, and non-BAL RQQs, plotted versus redshift. The RLQ comparison sample is constructed from SDSS/FIRST/*Chandra* data, supplemented with some particularly luminous RLQs observed by *Einstein* (Worrall et al. 1987). The BAL RQQ comparison sample is taken from Gibson et al. (2009) and is supplemented with non-SDSS objects from Gallagher et al. (2006). The RQQ comparison sample is taken from Gibson et al. (2008a) and is supplemented with luminous RQQs from Just et al. (2007). Quasars from the DR5 Quasar Catalog of Schneider et al. (2007) are shown as gray points. Our *Chandra* snapshot sample is biased toward luminous quasars as a consequence of the magnitude-limited selection method. The comparison samples have been constructed to overlap and bracket the BAL RLQs in optical luminosity and redshift.

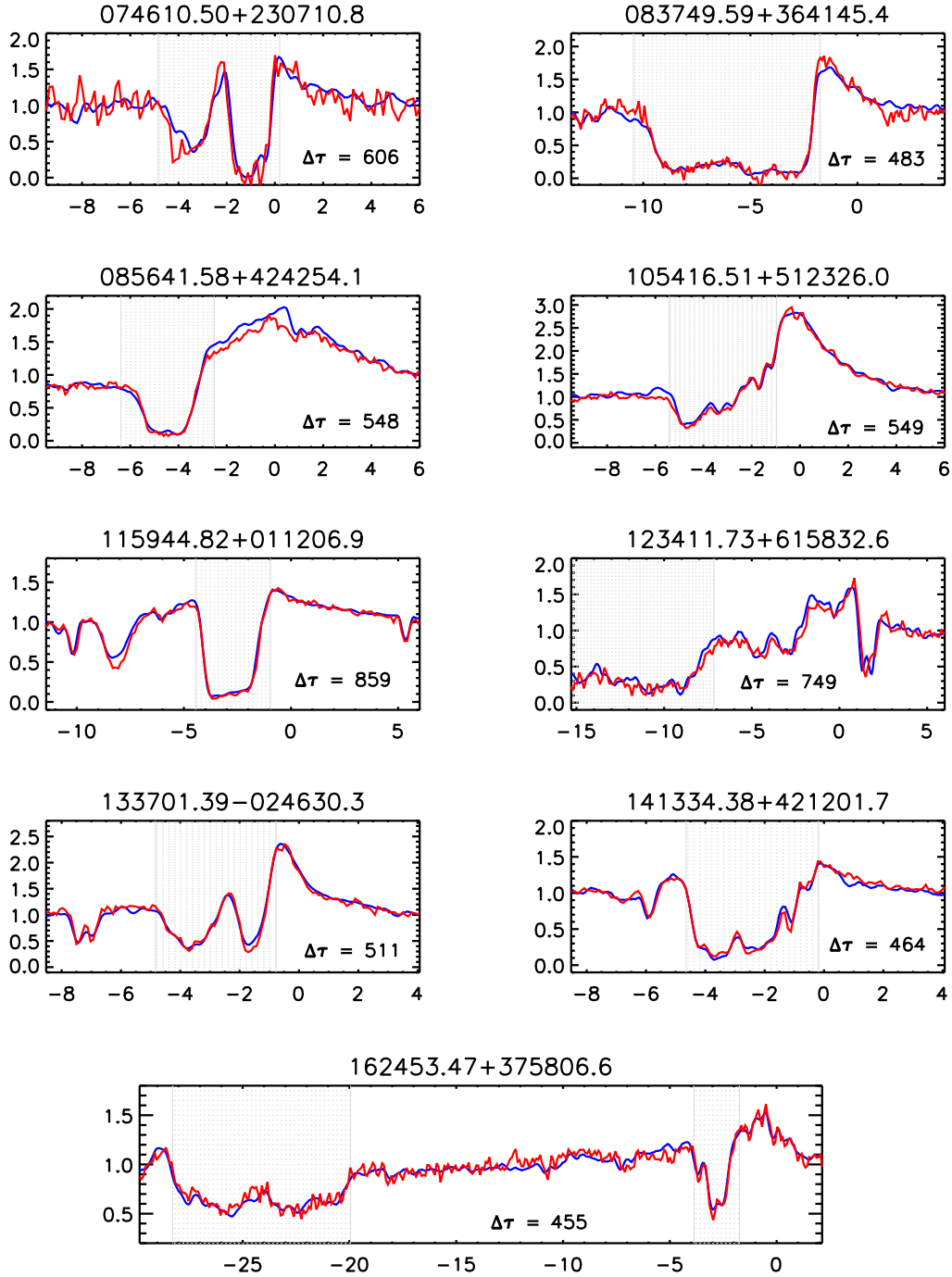


Fig. 6.— HET/LRS spectra (red lines) taken near the times of the *Chandra* snapshot observations, shown compared to the earlier epoch SDSS spectra (blue lines) matched to HET/LRS resolution. Each panel is labeled with the SDSS DR5 name as well as the rest-frame interval between observations (in days). The horizontal axis is velocity in  $1000 \text{ km s}^{-1}$  and the vertical axis is normalized flux. The C IV absorption regions are shaded gray. There is only minor BAL variability seen in these objects, indicating that variability does not significantly complicate a comparison of UV absorption properties to X-ray weakness.



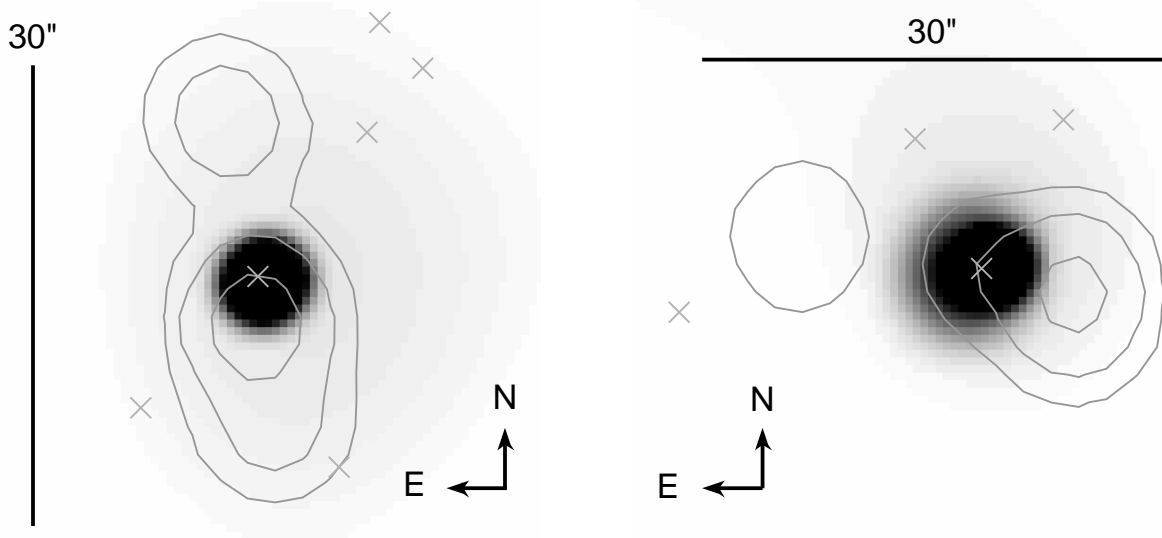


Fig. 7.— *Chandra* images of the two BAL RLQs in the snapshot survey possessing extended radio emission. The left panel shows J102258.41+123429.7; the right panel shows J112506.95-001647.6. For both objects  $30''$  is  $\simeq 250$  kpc. Adaptively smoothed 0.5–8 keV images are plotted in grayscale with logarithmic scaling, overlaid with contours from the 5 GHz FIRST survey at levels of 2, 8, and 32  $\text{mJy beam}^{-1}$ . Peak fluxes for the radio sources are  $< 85\%$  of the integrated fluxes and the deconvolved major axes are  $\sim 3 - 5''$ ; FIRST apparently resolves these components. The crosses mark SDSS photometric sources within the field; none of these aligns with the apparent extended radio emission, further indicating that these are lobes rather than unrelated sources.

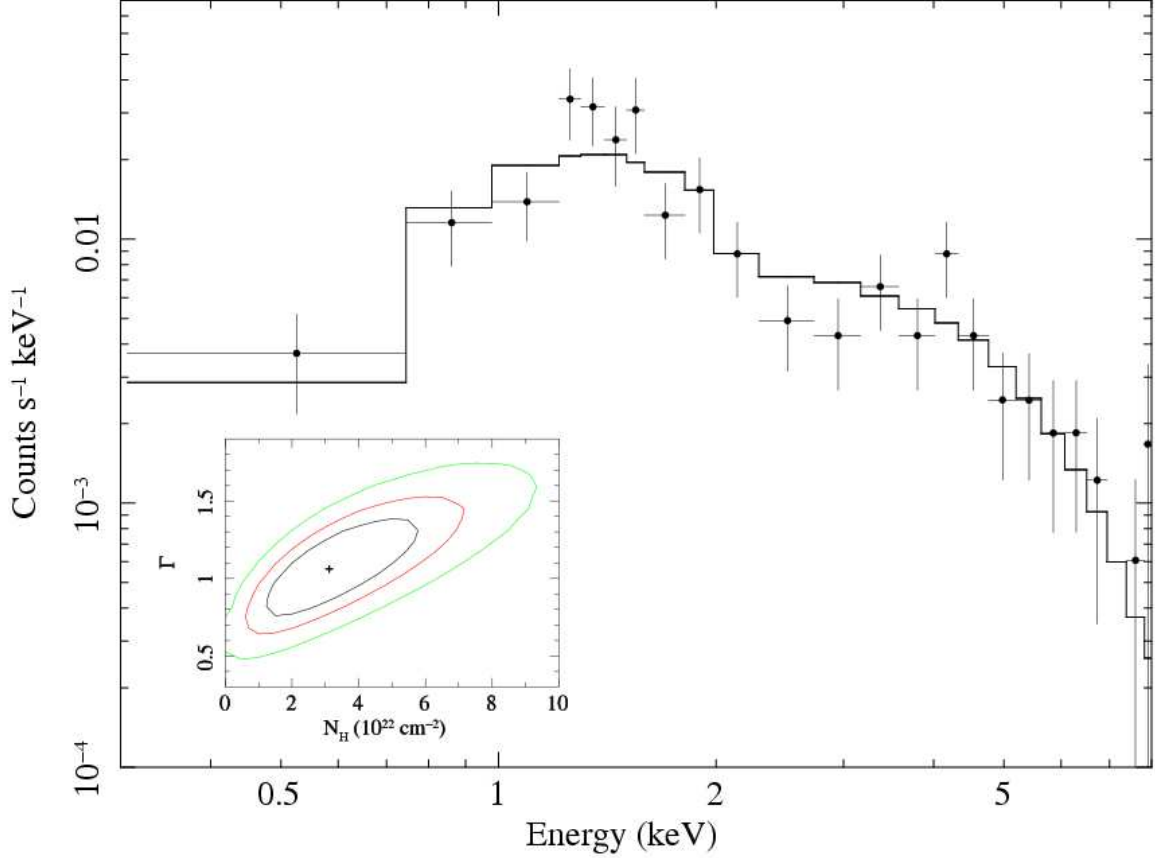


Fig. 8.— *Chandra* spectrum of J115944.82+011206.9, the X-ray brightest source in our snapshot sample with  $\simeq 170$  counts from 0.3–8 keV ( $\sim 2\times$  that of the next-brightest snapshot BAL RLQ). The plotted model has intrinsic absorption with column density  $N_{\text{H}} = 3.2^{+2.9}_{-2.1} \times 10^{22} \text{ cm}^{-2}$  and a power-law photon index of  $\Gamma = 1.06^{+0.35}_{-0.33}$ . The fit was performed using the *cstat* statistic and the cosmetic binning is based on a minimum significance of  $3\sigma$  within a maximum of 30 bins. The inset shows the 68, 90, and 99% confidence contours (for two parameters of interest) for the photon index  $\Gamma$  and intrinsic column density  $N_{\text{H}}$ .

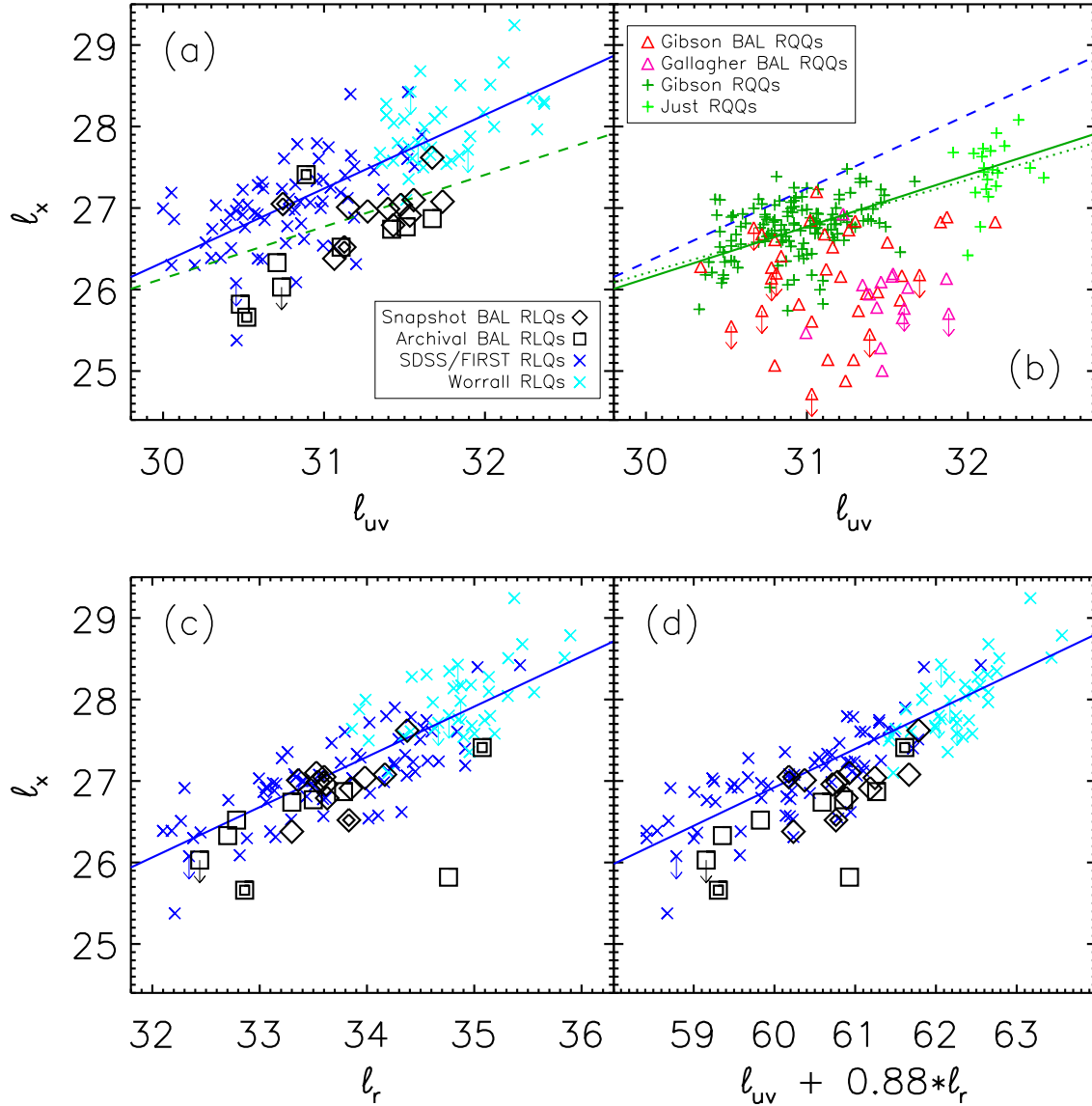


Fig. 9.— X-ray luminosities of BAL quasars compared to similar non-BAL quasars. Luminosities have units of  $\log \text{ ergs s}^{-1} \text{ Hz}^{-1}$ , at rest-frame frequencies of 5 GHz, 2500 Å, and 2 keV for  $l_r$ ,  $l_{uv}$ , and  $l_x$ , respectively. Arrows indicate X-ray upper limits, and nested symbols are lobe-dominated BAL RLQs. Blue lines are best-fit correlations for non-BAL RLQs (taking  $l_x$  as the dependent variable) calculated using the Bayesian maximum-likelihood method of Kelly (2007). The solid green line shows the best-fit correlation for non-BAL RQQs that Just et al. (2007) calculated with ASURV for a large sample of RQQs; fitting our comparison sample of RQQs yields a similar result (dotted green line). The  $l_x(l_{uv})$  relation for RLQs/RQQs is also plotted as a dashed line in (b)/(a), illustrating the well-known tendency for RLQs to be X-ray brighter than comparable RQQs. BAL RLQs are X-ray weak relative to non-BAL RLQs with similar optical/UV luminosities (a) but not to the same degree as are BAL RQQs relative to non-BAL RQQs (b). BAL RLQs are also modestly X-ray weak relative to non-BAL RLQs with similar radio luminosities (c) and to non-BAL RLQs with both similar optical/UV and radio luminosities (d).

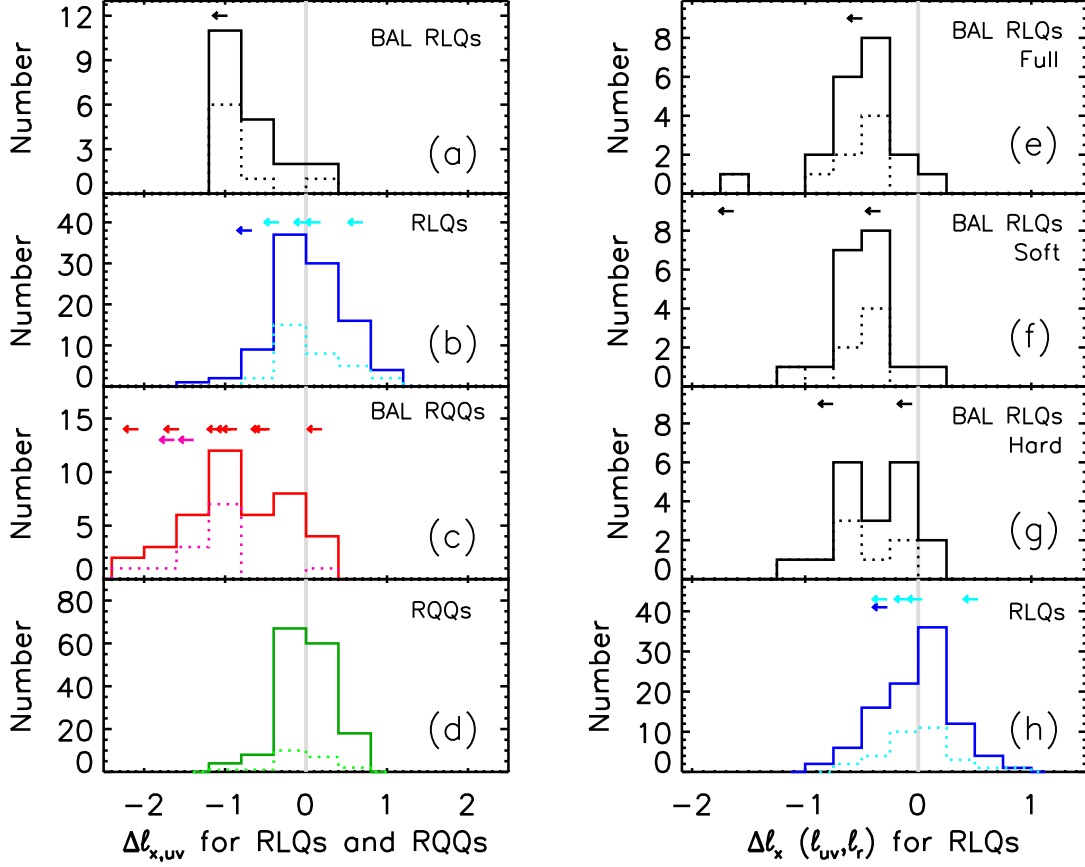


Fig. 10.— Histograms showing the distribution of the difference between actual and anticipated X-ray luminosity. Arrows indicate X-ray limits. Dotted histograms show subsamples: archival BAL RLQs (black), Worrall et al. (1987) RLQs (cyan), Gallagher et al. (2006) BAL RLQs (magenta), and Just et al. (2007) RQQs (light green). The left column (a, b, c, d) shows  $\Delta l_{x,uv}$  calculated from optical/UV luminosities using the relations shown in Figures 9a and 9b. BAL RQQs reach more extreme values of X-ray weakness relative to non-BAL RQQs than do BAL RLQs relative to non-BAL RLQs with similar optical/UV luminosities. The right column (e, f, g, h) shows  $\Delta l_x$  calculated from both optical/UV *and* radio luminosities for RLQs, using the relation shown in Figure 9d. X-ray luminosity is calculated using the full (0.5–8 keV), soft (0.5–2 keV), and hard (2–8 keV) counts. BAL RLQs are typically X-ray weaker than comparable non-BAL RLQs by a factor of 2.0–4.5. The similarity of results derived using full, soft, and hard X-ray luminosities suggests simple absorption of the entire X-ray continuum source cannot provide a universal explanation for the X-ray weakness in BAL RLQs.

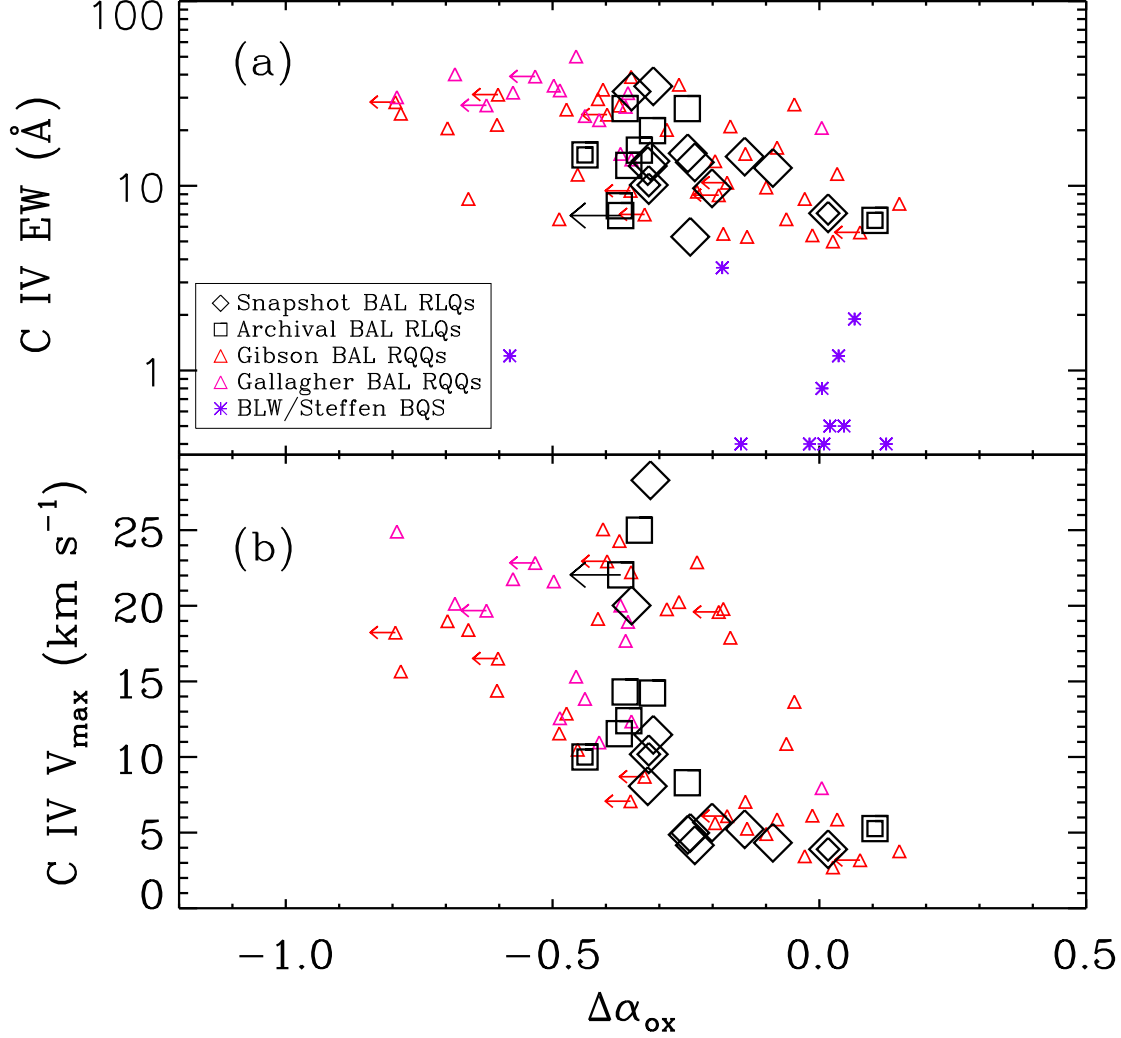


Fig. 11.— C IV absorption properties as a function of relative X-ray luminosity, calculated using the relations shown in Figures 9a and 9b and expressed in terms of  $\Delta\alpha_{\text{ox}}(l_{\text{uv}})$ , where  $\alpha_{\text{ox}} = 0.384 \times (l_{\text{x}} - l_{\text{uv}})$ , for ease of comparison with previous work. Panel (a) shows C IV EW and (b) shows maximum outflow velocity. Nested symbols are lobe-dominated BAL RLQs. The purple points in (a) are non-BAL RQQs from the BQS, with C IV absorption values from Brandt, Laor, & Wills (2000) and optical and X-ray luminosities from Steffen et al. (2006). X-ray weakness appears more closely linked to absorption strength in BAL RQQs than in BAL RLQs; even BAL RLQs with extreme C IV absorption properties do not have  $\Delta\alpha_{\text{ox}} < -0.5$ , as do many strongly absorbed BAL RQQs.

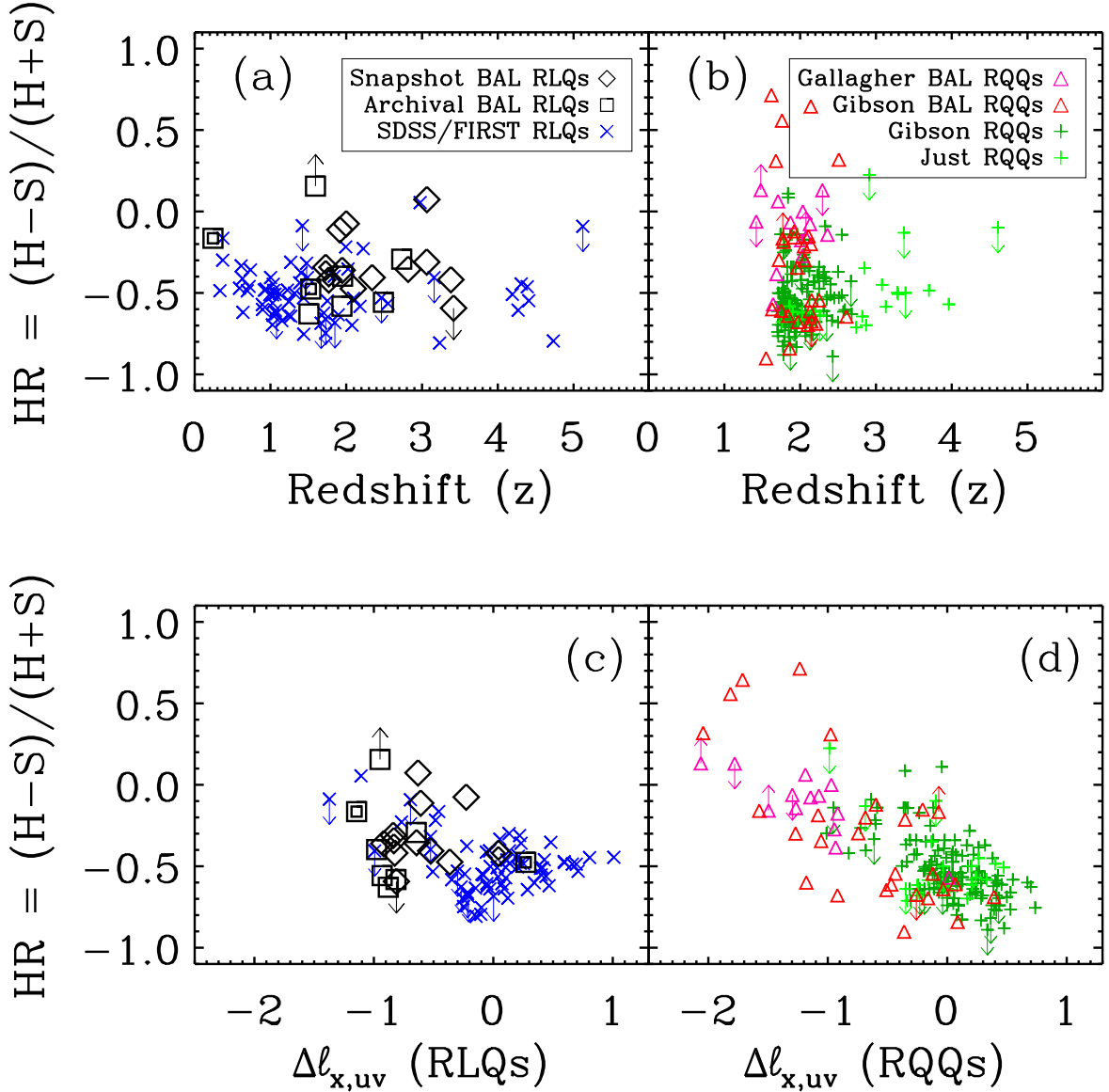


Fig. 12.— Hardness ratio plotted versus redshift for the sample of BAL RLQs (nested symbols are lobe-dominated BAL RLQs) and for comparison samples of RLQs (a) and for BAL RQQs and RQQs (b). The X-ray spectra of BAL RLQs are sometimes harder than those of typical non-BAL RLQs, but are often consistent. The X-ray spectra of BAL RQQs are often harder than for typical non-BAL RQQs, reaching extreme hardness ratios in some cases, and the distribution of hardness ratios for BAL RQQs is not statistically consistent with that of RQQs. Panels (c) and (d) show hardness ratio plotted versus  $\Delta l_{x,uv}$  calculated using the relations shown in Figures 9a and 9b; the X-ray weakness of BAL RQQs is linked to increasing intrinsic absorption of the continuum (illustrated via harder X-ray spectra), while many X-ray weak BAL RLQs do not have extremely hard X-ray spectra.

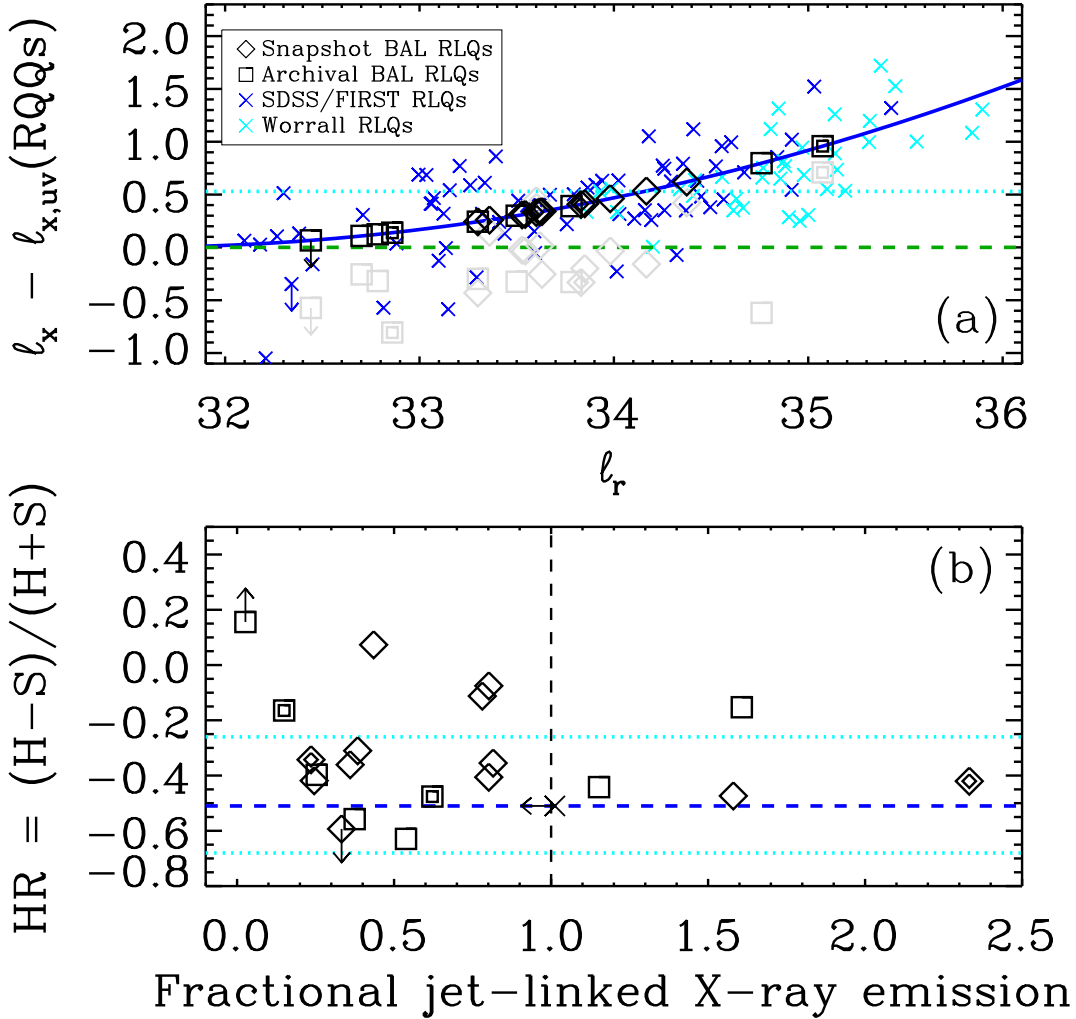


Fig. 13.— The top panel (a) shows the ratio of X-ray luminosity in RLQs to that of RQQs with comparable optical/UV luminosities, expressed in log units, as a function of radio luminosity. The median factor by which the comparison sample of RLQs are X-ray brighter than the comparison sample of RQQs is 3.4 (cyan dashed line); there is a trend (illustrated with the solid blue line) toward increasing X-ray brightness with increasing radio luminosity that likely reflects increasing jet dominance. BAL RLQs are plotted at their predicted (black) and observed (gray) X-ray luminosity ratios (nested symbols are lobe-dominated BAL RLQs). The bottom panel (b) shows the fraction of jet-linked X-ray emission in BAL RLQs relative to that expected for non-BAL RLQs with similar optical/UV and radio luminosities, assuming the disk/corona X-ray emission (predicted from the optical/UV luminosity using the RQQ relation) is reduced by a factor of 10, as is typical for BAL RQQs. Values for the fractional jet-linked emission near (or above) 1 would suggest the jet is unobscured, while values near 0.1 would indicate the jet is covered and reduced in intensity to a similar degree as is the disk/corona emission. The median, 10th, and 90th percentile values of hardness ratio for RLQs are also plotted (blue dashed and cyan dotted lines, respectively).

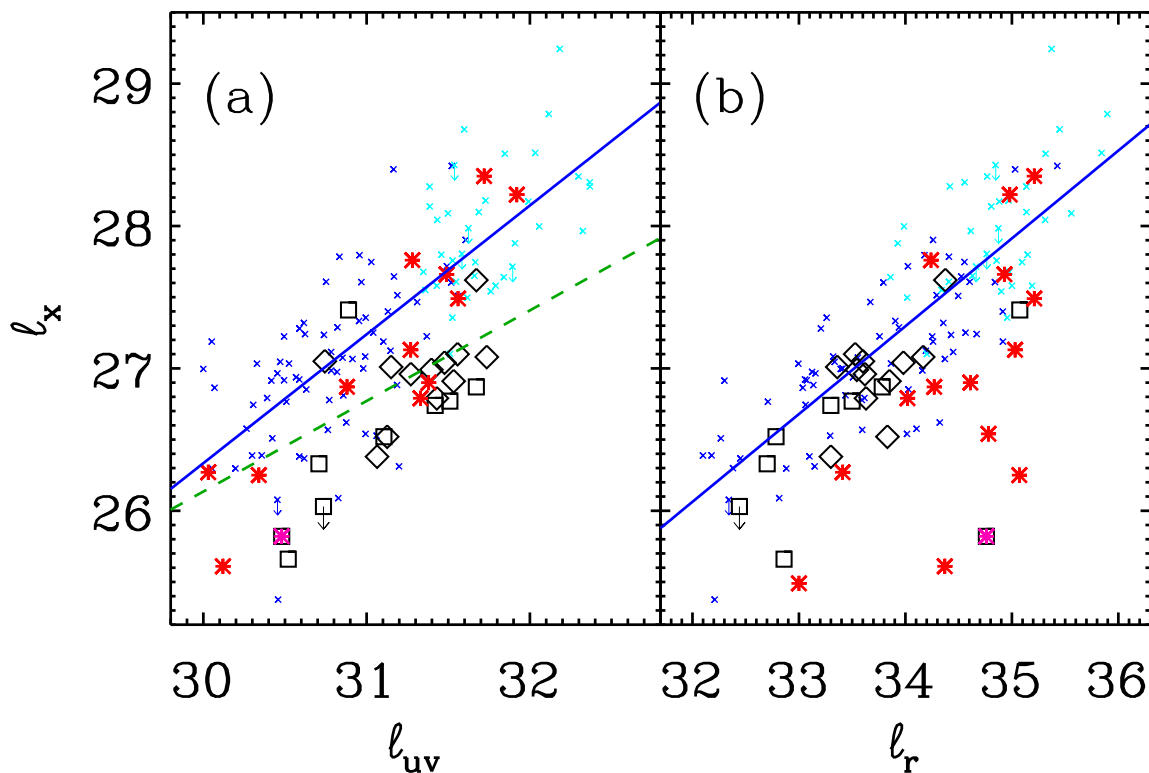


Fig. 14.— Comparison of the luminosities of GPS and CSS sources to those of BAL RLQs and non-BAL RLQs. Data for GPS and CSS sources (red stars) are from Siemiginowska et al. (2008). The legend and caption for BAL RLQs and non-BAL RLQs is identical to Figures 9a and 9c for (a) and (b), respectively. The  $l_x(l_{uv})$  relation for non-BAL RLQs from Figure 9b is shown as a dotted green line in (a). The CSS BAL RLQ J104834.24+345724.9 is indicated with a magenta star.